ELSEVIER

Contents lists available at ScienceDirect

Wave Motion

journal homepage: www.elsevier.com/locate/wamot



Prediction of local resonance band gaps in 2D elastic metamaterials via Bloch mode identification



A. Ragonese, M. Nouh*

Mechanical and Aerospace Engineering Dept., University at Buffalo (SUNY), Buffalo, NY 14260, USA

ARTICLE INFO

Article history: Received 20 September 2020 Received in revised form 18 February 2021 Accepted 6 April 2021 Available online 21 April 2021

Keywords: Metamaterial Local resonance Band gap System identification

ABSTRACT

This paper investigates methods of band gap formation in two-dimensional locally resonant elastic metamaterials and proposes a technique for computing such gaps as algebraic functions of integrated Bloch modes and metamaterial parameters. Mode shapes associated with the deformation of unit cells consisting of a hard matrix, soft filler, and hard resonator are investigated near the lower and upper bounds of the first local resonance band gap. Similarities reveal that Bloch modes at these bounds have the same non-dimensional geometries and locations within the irreducible Brillouin Zone irrespective of material properties, matrix and resonator thicknesses, and unit cell size. A theoretical model for the unit cell incorporating Mindlin plate theory is employed to compute the frequency of these modes in transverse vibration using conservation of energy. A least squares system identification algorithm is then described to generate surface equations for non-dimensional Bloch mode shapes computed by finite element analysis, employing a computation-saving Kronecker factorization and yielding continuous surface equations for the non-dimensional Bloch modes when rectangular cell components are utilized. Nine sample metamaterials are analyzed with this approach generating reliable predictions of the first band gap bounds. The presented framework offers insights into band gap formation, opens avenues in inverse unit cell design, and provides versatile algebraic relationships between band gap frequencies and unit cell parameters in such resonant metamaterials.

© 2021 Elsevier B.V. All rights reserved.

1. Introduction

Elastic metamaterials with locally resonant components have grown increasingly popular in applications requiring vibration isolation and mitigation of external loads, due largely to their ability to create subwavelength band gaps (BGs) in frequency domains much lower than non-resonant metamaterials of similar size [1–7]. The phenomenon, which was first presented by Liu et al. [8], has sparked numerous investigations into methods of BG formation and guidelines for designing metamaterials with specific BGs in various locally resonant geometries [9–13]. Sugino et al. [14] for example analyzed a one-dimensional locally resonant metamaterial beam with discrete spring–mass resonators and derived a concise formula for computing the first (lowest-frequency) BG using a modal analysis approach, providing a guideline for designing such a geometry to attain a specific BG. Peng and Pai [15] conducted a related study on elastic metamaterial plates with discrete spring–mass absorbers and found that the location of the BG depends on the natural frequency of the local resonators, while the width of the BG increases as the ratio of the resonator mass to the total unit cell mass increases.

E-mail address: mnouh@buffalo.edu (M. Nouh).

^{*} Corresponding author.

Krushynska et al. [16] investigated the topic of locally resonant elastic metamaterial plates with continuous "hard-soft-hard" (H–S–H) configurations analyzing the effects of varying unit cell parameters on the dispersion band spectra for both in- and out-of-plane vibrations and proposing a design strategy for obtaining an optimal metamaterial with specific BG properties. They further expanded the analysis to distinguish between different resonant inclusions [17]. The focus of this effort will be on such H–S–H metamaterials. Our interest in these configurations stems from their manufacturability and their ability to attenuate low-frequency vibrations which are incident from any direction (e.g., [2]). However, the two-dimensional nature and higher-order analytical and finite element models required to predict the performance of such metamaterials render the analysis both more complex and computationally expensive. As a result, investigations into BG formation mechanisms in metamaterials with such geometries are naturally more difficult to achieve than in 1D and discrete spring–mass resonant counterparts.

Motivated by the previous challenges, we consider locally resonant H–S–H metamaterials in this paper in a slightly different light by focusing on similarities between Bloch wave modes of such metamaterials, proposing a novel technique for BG computation, and offering further insights into BG formation in such metamaterials. Unlike conventional structures, which are finite in length and defined by boundary conditions, metamaterials are typically modeled as infinite arrangements of a series of building blocks, commonly referred to as "unit cells", owing to the periodic (i.e., self-repeating) nature of these cells [18,19]. H-S-H unit cells in particular consist of a dense, resonating element embedded within a soft filler material that is itself embedded within a stiff rectangular matrix, with multiple repeated unit cells in a one- or twodimensional array comprising the metamaterial (Fig. 1). Analogous to vibrational modes of finite structures, Bloch modes depict the deformation patterns (and frequencies thereof) of such unit cells at prescribed points within their dispersion diagrams [20]. To compute the BGs of such structures, the prevailing method relies on a finite element eigenfrequency dispersion analysis of an individual self-repeating unit cell conducted along the boundary of the irreducible Brillouin zone (IBZ), simulating an infinite structure by varying wavenumbers in the x- $(\tilde{k}_x = ak_x)$ and y- $(\tilde{k}_y = bk_y)$ directions. Here, \tilde{k}_x and \tilde{k}_y denote the non-dimensional wavenumbers (periodic with period 2π) in the x- and y-directions and a and b denote the unit cell dimensions (analogous to the lattice constants of a crystal). The frequency ranges for which no solutions at any wavenumber combination are computed define the BGs of the structure and are the hallmark feature of H-S-H and more general elastic metamaterials. A dispersion plot displaying the first few bands of the band structure as well as the first BG for the unit cell in Fig. 1b is displayed in Fig. 1c, computed using finite element eigenfrequency analysis (FEEA) for a 20 \times 20 mesh of quadrilateral, 12-node planar cubic elements and 200 points along the M- Γ -X-M IBZ boundary. However, despite the proven promise of FEEA in BG computation of H-S-H metamaterials, there are a number of less-than-optimal considerations about FEEA combined with similarities between the band structures and Bloch modes in H-S-H geometries that suggest a potentially novel analytical approach to BG computation in such metamaterials.

Although FEEA has been undoubtedly shown to be an incredibly versatile and accurate method of BG computation in H–S–H metamaterials ([2,16] to name a few), it remains a computationally-expensive method that does not lend itself well to *on-demand* design of metamaterials with targeted or desired BGs. For instance, when calculating BGs of elastic metamaterials by FEEA, the frequency bands of the dispersion plot generated by the analysis are always defined by discrete points (rather than a smooth function), requiring numerous repetitions of the analysis at small wavenumber intervals when a fine dispersion profile (and therefore, accurate BG calculation) is desired, which leads to potentially lengthy computation times especially for systems comprising large numbers of degrees of freedom (DOFs). More importantly, BGs determined by FEEA do not provide information on the sensitivity of the calculation to changes in material properties, unit cell size, or geometry (e.g., the thickness of the matrix or resonator elements of the unit cells), making FEEA less-than-reasonable as a method when parametric studies of many designs are undergone to determine the optimal parameters of a metamaterial with specific BGs. Krushynska et al. [16] presented an ideal example of this by parametrically varying the sizes of filler and resonator elements in H–S–H metamaterials to determine the effects of such variation on the metamaterial's BG frequencies; however, the BGs of each solution were still obtained with finite element analyses.

To this end, the objective of this paper is two-fold. First, we identify and outline a few critical similarities which exist between the dispersion band structures and Bloch modes of H–S–H metamaterials. Second, we strategically exploit these similarities to devise a novel computationally-efficient algorithm for computing BGs in H–S–H metamaterials, using system identification of Bloch mode shapes. To do this, Section 2 describes two critical observations between Bloch modes and dispersion band structures in H–S–H metamaterials that provide the fundamental motivation for the present method. Section 3 presents an approach for computing the frequency of an elastic metamaterial unit cell vibrating with a particular Bloch mode, guided by observations from the previous section. Following this, a Least Squares Identification Algorithm is detailed in Section 4 to identify surface equations for unit cell Bloch mode shapes that can be directly employed to compute metamaterial BGs using the derivations in Section 3. A numerical example demonstrating the utility of the novel method is presented in Section 5, and a procedure for designing a metamaterial with a specified BG using algebraic relationships between unit cell parameters is detailed in Section 6. Finally, Section 7 summarizes the analysis and outlines possible extensions of this work in various metamaterial applications.

2. Observing Bloch modes in H-S-H metamaterials

In elastic metamaterials, *Bloch modes* refer to mode shapes corresponding to elastic wave propagation in an individual unit cell of an infinitely long periodic structure, as opposed to the traditional vibration mode shapes of a finite structure

under a set of prescribed boundary conditions [20,21]. For elastic metamaterial plates analyzed using Mindlin plate theory (our theory of choice and applied in Section 3), these Bloch modes take the form of displacement, *x*-rotation, and *y*-rotation surfaces defined over the planar area of the unit cell, as will be detailed later. A few critical similarities between the Bloch modes and dispersion band structures of H–S–H metamaterials can be established that provide insight into the method of BG formation and motivation for a novel approach to BG computation in such structures. Two essential observations of H–S–H metamaterials are presented in this section that contribute to this novel method.

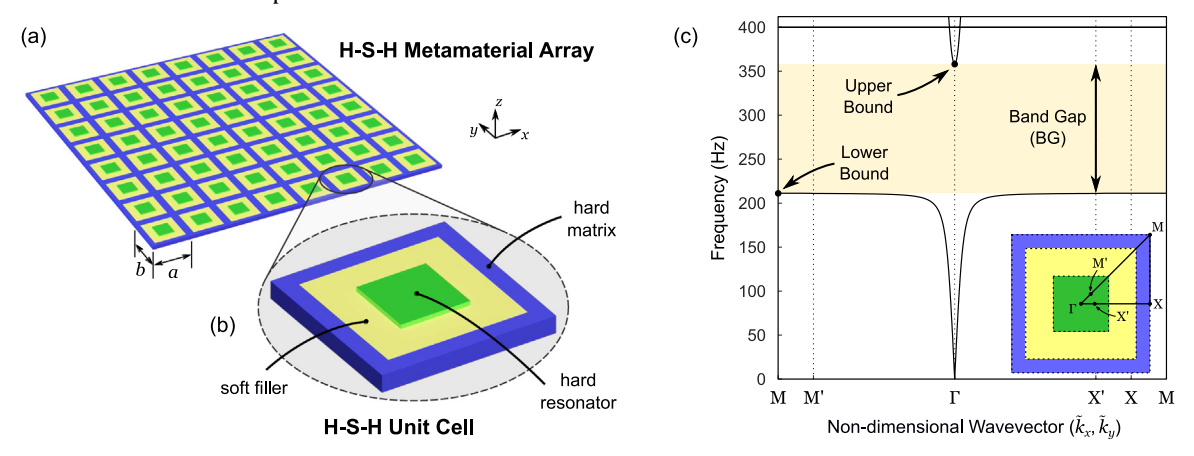


Fig. 1. Hard-soft-hard (H–S–H) locally resonant metamaterials: (a) 2D array and (b) unit cell of an H–S–H metamaterial in transverse vibration. Waves propagate in the *xy*-plane of the metamaterial; material displacements occur in the *z*-direction. (c) Dispersion band structure identifying the two lowest frequency bands and the first band gap (shaded region) for an H–S–H metamaterial. The inset in the bottom right depicts the metamaterial unit cell and wavenumber positions at the M, Γ , and X positions of the IBZ. Note the change in scale of the horizontal axis at the points M′ and X′.

2.1. Observation 1: Similarity in dispersion band structures

The first critical observation of H–S–H metamaterials motivating this analysis is that all transverse vibrations in the vicinity of the lower and upper limits of the first BG occur with the *same non-dimensional wavenumbers* for any combination of material properties, matrix or resonator thicknesses, and unit cell size, provided that the elastic modulus of the filler material is sufficiently smaller than that of the matrix material. This requirement is easily satisfied by the many H–S–H metamaterials that use very soft silicone rubber as the filler material—e.g., [2,8,16]. That is, the modes of vibration in the pass band immediately below and above the first BG occur at the same location of the IBZ in all H–S–H metamaterials containing relatively rigid matrix and resonator elements (enabled by soft filler material) and a given thickness of the filler material relative to the unit cell size. The only exception to this observation occurs when the matrix element becomes very light (or thin) or the resonator becomes extremely dense (or thick), which has the potential to cause a flat, single-frequency band separating the first BG into two regions (this will be illustrated with a numerical example in Section 5). However, when treated as a single BG with an intermediate resonance frequency, the lower bound of the first separated BG and the upper bound of the second separated BG still meet this observation (in these cases, the combined BG between the two separated BGs will be referred to as the "first BG" in this paper).

A graphical illustration of this observation is presented in Fig. 1c, depicting a typical dispersion band structure around the IBZ boundary for a sample H–S–H metamaterial shown in the inset portion of the figure. In particular, it can be observed that the lower bound of the first BG is associated with the M point of the IBZ (defined by non-dimensional wavenumbers $\tilde{k}_x = \tilde{k}_y = \pi$), and the upper bound is associated with the Γ point of the IBZ (defined by non-dimensional wavenumbers $\tilde{k}_x = \tilde{k}_y = 0$) for this and all other H–S–H metamaterials of soft filler material. As a result, the lower and upper bounds of the first BG of such a metamaterial can be calculated by performing FEEA at *only the* M *and* Γ *points* of the IBZ, rather than along the entire IBZ boundary. This observation tremendously simplifies the analysis of such metamaterials when knowledge of the first BG is desired—however, it does not provide insight into the sensitivity of the BG frequency or bandwidth to the material properties, unit cell size, or element thicknesses of the metamaterial. The second observation and the remainder of the paper are intended to address this second issue.

2.2. Observation 2: Similarity in Bloch modes

The second observation motivating this analysis is that *all transverse vibrations* propagating in H–S–H metamaterials of soft filler material at the M and Γ points of the IBZ and at frequencies just beyond the limits of the first BG occur with the *same Bloch modes* for any combination of material properties, matrix or resonator thicknesses, and unit cell size for a given reference geometry, where "reference geometry" is used to refer to the cross section of the unit cell in the *xy*-plane normalized by the unit cell dimension (a or b) and the thickness of the filler material relative to this dimension.

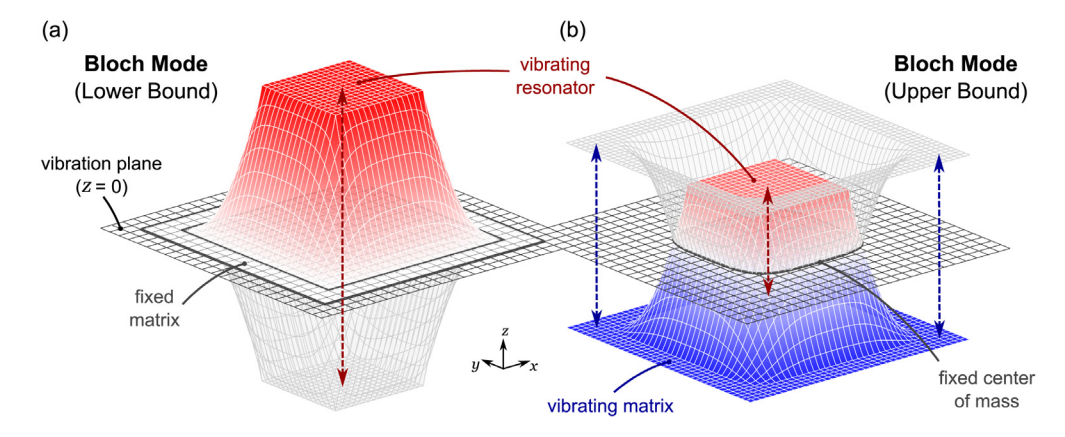


Fig. 2. Displacement Bloch mode shapes at the (a) lower bound and (b) upper bound of the first BG of a sample H-S-H metamaterial.

(Unit cells of different relative filler thicknesses are observed to not follow this phenomenon, since the difference in filler thickness relative to the size of the cell institutes a different non-dimensional shape to the Bloch modes due to the large deformations present in the soft filler material). Stated differently, all H–S–H metamaterials with a specific reference geometry and soft filler material vibrate with the same Bloch modes at the natural frequencies corresponding to the lower and upper limits of the first BG. This observation can be made by conducting FEEA for an H–S–H unit cell to plot the first few bands of the band structure along the IBZ boundary (both COMSOL Multiphysics and an in-house MATLAB code were used here), verifying that the BG limits indeed occur at the M and Γ points of the IBZ, and generating the displacement and rotation Bloch modes at the appropriate M and Γ frequencies corresponding to these BG limits on the dispersion band structure. Therefore, given a specific reference geometry and by varying any or all of the material properties, matrix or resonator thicknesses, or unit cell size of the metamaterial (while retaining the soft filler material compared to the matrix and resonator elements), it can be observed that both the non-dimensional wavenumbers at the BG limits and the general shapes of the Bloch modes *do not change* when any of these metamaterial parameters are altered.

To illustrate this observation, the general displacement Bloch modes at the lower and upper bounds of the first BG for the metamaterial in Fig. 1 are displayed in Fig. 2, depicting the transverse vibration of the unit cell with sample reference geometry at the lower (Fig. 2a) and upper (Fig. 2b) limits of the first BG. After repeated investigations of H–S–H metamaterials analyzed with FEEA, it can be observed that the displacement Bloch mode at the lower bound of the first BG is always characterized by a rigid, vibrating resonator moving about a rigid, fixed matrix via a periodically deforming and relaxing filler material, as illustrated in Fig. 2a. Similar observations reveal that the upper bound of the first BG is always characterized by a rigid resonator and a rigid matrix vibrating out-of-phase with each other about a deforming filler material and moving about the center of mass of the vibrating unit cell, as illustrated in Fig. 2b. Both of these Bloch modes are observed to have the same mode shape and occur with the same non-dimensional wavenumbers irrespective of the material properties, unit cell size, or thicknesses of the matrix and resonator elements (changes in filler thickness are allowed as well as long as they are made in proportion to changes in unit cell size), providing a pragmatic unification between all H–S–H metamaterials with soft filler material and specific reference geometry.

Given these similarities in dispersion band structures and Bloch modes in H–S–H metamaterials, it would be possible to estimate the limiting frequencies of the first BG for any H–S–H metamaterial of specific reference geometry using a *single finite element eigenfrequency analysis* if a method existed for determining the vibration frequency of a unit cell vibrating with specific Bloch modes in terms of the metamaterial's unit cell size, material properties, and element thicknesses, along with data from a single FEEA describing the Bloch modes at the BG bounds for that geometry. A technique for doing this is the subject of the remainder of this paper, with Section 3 describing a method for computing the vibration frequency of a unit cell with known continuous Bloch modes and Section 4 detailing a procedure for determining continuous surface equations for Bloch modes from finite element data with a system identification procedure.

3. Computing natural frequencies using Bloch modes

As previously demonstrated, the observation that all H–S–H metamaterials with a given reference geometry and sufficiently soft filler material share the same Bloch modes at the limits of the first transverse frequency BG has significant implications in drawing parallels between the first BGs of H–S–H metamaterials. Most notably: if the Bloch modes shared by these metamaterials are calculated by a single FEEA, could there be a method of determining the vibration frequency of other metamaterials having those same Bloch modes—and hence, the frequency limits of the first BG in those metamaterials—with only a single FEEA? The answer to this question is definitely affirmative, and it will be shown in the following analysis how a novel computational approach for the first transverse frequency BG can be developed using analysis of Bloch modes and a system identification procedure.

We start by deriving a method for calculating the vibration frequency of an elastic metamaterial unit cell corresponding to specific Bloch modes, which plays an important role in the overall BG computation algorithm. The method is achieved via an analysis of the potential and kinetic energies in a unit cell subject to periodic vibration and the assumptions of Mindlin plate theory. The z-directional displacement w and the angular displacements θ_x and θ_y about the x- and y-axes are adopted as the independent kinematic variables in the unit cell, with the remaining translational variables u and v computed using θ_x and θ_y as described in Eq. (1). The remaining angular displacement θ_z about the z-axis is equal to zero in accordance with Mindlin plate theory and our restriction to out-of-plane material motion (Fig. 3) [22–24]. Further, it is assumed that each unit cell may be treated as a control volume with negligible damping governed by the classical law of conservation of energy, and that each unit cell vibrates in a sinusoidal manner (a feature of any general plate vibration model). Using these assumptions, Sections 3.1 and 3.2 describe integral relations for the maximum potential and kinetic energies in the vibrating unit cell that can be obtained in terms of non-dimensional Bloch modes describing the vibration at the BG bound and the unit cell's material and geometric properties. Following this, Section 3.3 presents a conservation of energy argument using these potential and kinetic energies to provide a simple equation for calculating the vibration frequency (and thus—a frequency bound of the BG) of the H–S–H unit cell as a function of material properties, unit cell geometry, and continuous equations for the non-dimensional Bloch modes defining the vibration.

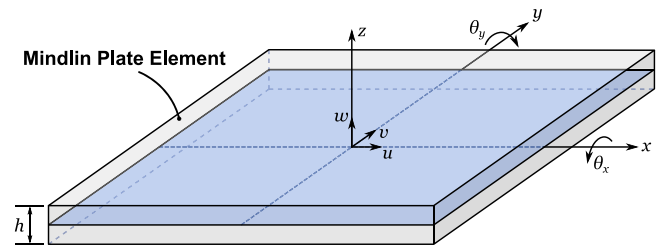


Fig. 3. Mindlin plate element defining the five kinematic variables u, v, w, θ_x , and θ_y in their positive directions for an elastic metamaterial. The x- and y-displacements can be written as functions of z and the rotational displacements θ_x and θ_y as per Eq. (1), leaving w, θ_x , and θ_y as the independent kinematic variables defined over the mid-planar region of the unit cell.

3.1. Potential energy analysis

Consider an H–S–H unit cell vibrating with non-dimensional Bloch modes W(x,y), $\Theta_x(x,y)$, and $\Theta_y(x,y)$, where W is the displacement Bloch mode (the amplitude of the z-displacement w), Θ_x is the x-rotation Bloch mode (the amplitude of the x-rotation θ_x), and Θ_y is the y-rotation Bloch mode (the amplitude of the y-rotation θ_y), where "non-dimensional" denotes the fact that W, Θ_x , and Θ_y are each normalized to provide a constant, dimensionless description of the Bloch modes for any unit cell size (Eqs. (13) and (14)). Further, suppose that any point in the unit cell in the mid-plane of the metamaterial can be represented by the Mindlin plate element shown in Fig. 3, in which the xy-plane defines the mid-plane of the metamaterial plate, the z-direction is the direction of transverse vibration, u(x,y,z,t), v(x,y,z,t), and w(x,y,t) are the displacements of the unit cell in the x-, y-, and z-directions, and $\theta_x(x,y,t)$ and $\theta_y(x,y,t)$ are the rotational counter-clockwise displacements about the x- and y-axes. (Note that the z-displacement w and the rotations θ_x and θ_y do not depend on z according to Mindlin plate theory). The goal of this section is to use this coordinate framework to determine the maximum potential energy in the vibrating unit cell as a function of the material properties, element thicknesses, and non-dimensional Bloch modes for a particular mode of vibration.

According to Mindlin plate theory, the displacements u and v can be written in terms of z, θ_x , and θ_y from geometry and a small angle approximation on θ_x and θ_y as

$$u = z\theta_{\rm v}$$
 and $v = -z\theta_{\rm x}$ (1)

Using Eq. (1) and the definition of bending strain $\epsilon_b \equiv [\epsilon_x \; \epsilon_y \; \gamma_{xy}]^T$, the bending strain in the unit cell can be expressed as a function of z and the spatial derivatives of θ_x and θ_y as

$$\epsilon_{b}(x, y, z, t) \equiv \begin{bmatrix} \epsilon_{x} \\ \epsilon_{y} \\ \gamma_{xy} \end{bmatrix} \equiv \begin{bmatrix} \frac{\partial u}{\partial x} \\ \frac{\partial v}{\partial y} \\ \frac{\partial v}{\partial x} + \frac{\partial u}{\partial y} \end{bmatrix} = z \begin{bmatrix} \frac{\partial \theta_{y}}{\partial x} \\ -\frac{\partial \theta_{x}}{\partial y} \\ -\frac{\partial \theta_{x}}{\partial x} + \frac{\partial \theta_{y}}{\partial y} \end{bmatrix}$$
(2)

Similarly, using Eq. (1) and the definition of transverse shear strain $\epsilon_s \equiv [\gamma_{xz} \ \gamma_{yz}]^T$, the transverse shear strain in the unit cell can be expressed as a function of θ_x , θ_y , and the spatial derivatives of w as

$$\epsilon_{s}(x, y, z, t) \equiv \begin{bmatrix} \gamma_{xz} \\ \gamma_{yz} \end{bmatrix} \equiv \begin{bmatrix} \frac{\partial w}{\partial x} + \frac{\partial u}{\partial z} \\ \frac{\partial w}{\partial y} + \frac{\partial v}{\partial z} \end{bmatrix} = \begin{bmatrix} \frac{\partial w}{\partial x} + \theta_{y} \\ \frac{\partial w}{\partial y} - \theta_{x} \end{bmatrix}$$
(3)

Letting the right side of Eq. (2) be equal to zL_b and the right side of Eq. (3) be equal to L_s , this yields the relations:

$$\epsilon_h = z \mathbf{L}_h \text{ and } \epsilon_s = \mathbf{L}_s$$
 (4)

where

$$\mathbf{L}_{b} \equiv \begin{bmatrix} \frac{\partial \theta_{y}}{\partial x} & -\frac{\partial \theta_{x}}{\partial y} & \left(-\frac{\partial \theta_{x}}{\partial x} + \frac{\partial \theta_{y}}{\partial y}\right) \end{bmatrix}^{\mathsf{T}} \text{ and } \mathbf{L}_{s} \equiv \begin{bmatrix} \left(\frac{\partial w}{\partial x} + \theta_{y}\right) & \left(\frac{\partial w}{\partial y} - \theta_{x}\right) \end{bmatrix}^{\mathsf{T}}$$
 (5)

Now consider the definitions of plane bending stress $\sigma_b \equiv [\sigma_x \ \sigma_y \ \tau_{xy}]^T = D_b \epsilon_b$ and transverse shear stress $\sigma_s \equiv [\tau_{xz} \ \tau_{yz}]^T = k_s D_s \epsilon_s$, where k_s is a shear correction factor accounting for the non-uniformity of the transverse shear stresses τ_{xz} and τ_{yz} over the domain of the unit cell (which typically holds a value of $k_s = \frac{5}{6}$ as in [2,25]), and the material property matrices D_b and D_s are defined as

$$D_b \equiv \frac{E}{1 - v^2} \begin{bmatrix} 1 & v & 0 \\ v & 1 & 0 \\ 0 & 0 & \frac{1 - v}{2} \end{bmatrix} \text{ and } D_s \equiv \frac{E}{2(1 + v)} \begin{bmatrix} 1 & 0 \\ 0 & 1 \end{bmatrix}$$
 (6)

in which E = E(x, y) and v = v(x, y) are the elastic (Young's) modulus and Poisson's ratio of the materials comprising the unit cell, respectively.

Next, let the elastic potential energy in the vibrating unit cell as a function of time be denoted by $\mathcal{V}(t)$, which can be expressed in terms of the bending stress, bending strain, transverse shear stress, and transverse shear strain integrated over the unit cell volume as

$$\mathcal{V}(t) \equiv \frac{1}{2} \int_{V} \left(\boldsymbol{\sigma}_{b}^{\mathsf{T}} \boldsymbol{\epsilon}_{b} + \boldsymbol{\sigma}_{s}^{\mathsf{T}} \boldsymbol{\epsilon}_{s} \right) dV = \frac{1}{2} \int_{V} \left(\boldsymbol{\epsilon}_{b}^{\mathsf{T}} D_{b} \boldsymbol{\epsilon}_{b} + k_{s} \boldsymbol{\epsilon}_{s}^{\mathsf{T}} D_{s} \boldsymbol{\epsilon}_{s} \right) dV \tag{7}$$

where the relations $\sigma_b = D_b \epsilon_b$ and $\sigma_s = k_s D_s \epsilon_s$ have been substituted to obtain the second equation. Substituting Eq. (4) for ϵ_b and ϵ_s simplifies this equation to

$$\mathcal{V}(t) = \frac{1}{2} \int_{\mathcal{V}} \left(z^2 \mathbf{L}_b^{\mathsf{T}} D_b \mathbf{L}_b + k_s \mathbf{L}_s^{\mathsf{T}} D_s \mathbf{L}_s \right) dV \tag{8}$$

which when split into an integral over the mid-planar area of the plate A and an integral over the plate thickness z yields

$$\mathcal{V}(t) = \frac{1}{2} \int_{A} \int_{-h/2}^{h/2} \left(z^2 \mathbf{L}_b^{\mathsf{T}} D_b \mathbf{L}_b + k_s \mathbf{L}_s^{\mathsf{T}} D_s \mathbf{L}_s \right) dz dA = \frac{1}{2} \int_{A} \left(\frac{h^3}{12} \mathbf{L}_b^{\mathsf{T}} D_b \mathbf{L}_b + k_s h \mathbf{L}_s^{\mathsf{T}} D_s \mathbf{L}_s \right) dA \tag{9}$$

where h = h(x, y) is the thickness of the elements comprising the unit cell. Next, substituting Eqs. (5) and (6) for \mathbf{L}_b , \mathbf{L}_s , D_b , and D_s into the expressions for $\mathbf{L}_b^T D_b \mathbf{L}_b$ and $\mathbf{L}_s^T D_s \mathbf{L}_s$ in Eq. (9) reveals that

$$\boldsymbol{L}_{b}^{\mathsf{T}}D_{b}\boldsymbol{L}_{b} = \frac{E}{1-\nu^{2}}\left(\left(\frac{\partial\theta_{y}}{\partial x}\right)^{2} - 2\nu\frac{\partial\theta_{y}}{\partial x}\frac{\partial\theta_{x}}{\partial y} + \left(\frac{\partial\theta_{x}}{\partial y}\right)^{2} + \left(\frac{1-\nu}{2}\right)\left(\frac{\partial\theta_{y}}{\partial y} - \frac{\partial\theta_{x}}{\partial x}\right)^{2}\right)$$
(10)

and

$$\boldsymbol{L}_{s}^{T}D_{s}\boldsymbol{L}_{s} = \frac{E}{2(1+\nu)}\left(\left(\frac{\partial w}{\partial x} + \theta_{y}\right)^{2} + \left(\frac{\partial w}{\partial y} - \theta_{x}\right)^{2}\right) \tag{11}$$

where typical matrix multiplication was employed to arrive at these equations. Substituting these expressions for $\boldsymbol{L}_b^{\mathrm{T}} D_b \boldsymbol{L}_b$ and $\boldsymbol{L}_s^{\mathrm{T}} D_s \boldsymbol{L}_s$ into Eq. (9) then yields

$$\mathcal{V}(t) = \frac{1}{2} \int_{A} \frac{Eh^{3}}{12(1-\nu^{2})} \left(\left(\frac{\partial \theta_{y}}{\partial x} \right)^{2} - 2\nu \frac{\partial \theta_{y}}{\partial x} \frac{\partial \theta_{x}}{\partial y} + \left(\frac{\partial \theta_{x}}{\partial y} \right)^{2} + \left(\frac{1-\nu}{2} \right) \left(\frac{\partial \theta_{y}}{\partial y} - \frac{\partial \theta_{x}}{\partial x} \right)^{2} \right) dA + \cdots$$

$$\cdots + \frac{k_{s}}{2} \int_{A} \frac{Eh}{2(1+\nu)} \left(\left(\frac{\partial w}{\partial x} + \theta_{y} \right)^{2} + \left(\frac{\partial w}{\partial y} - \theta_{x} \right)^{2} \right) dA$$

$$(12)$$

as an expression for the elastic potential energy as a function of time in the vibrating unit cell.

We now aim to determine the maximum value of Eq. (12) using a non-dimensional form of the displacement and rotation Bloch modes such that a specific set of Bloch modes generated from a single FEEA can be used to describe the metamaterial behavior for any unit cell size. Since the values of the z-displacement w remain unchanged with unit cell size for a given vibration amplitude, while the rotations θ_x and θ_y decrease in proportion to unit cell size for a given vibration amplitude, a factor of 1/a must be included in the relationship between θ_x and the x-rotation Bloch mode Θ_x and between θ_y and the y-rotation Bloch mode Θ_y , where a is the characteristic length (defined for completeness to be the maximum of the two side lengths) of the rectangular unit cell. Since w, θ_x , and θ_y each increase linearly as the vibration amplitude increases, a factor of d (defined to be the vibration amplitude) must also be included in the relationships between w and w, w, and w, and

assumed sinusoidally-periodic vibration of the unit cell. Using these relationships, the free kinematic variables w, θ_x , and θ_y can be expressed in terms of a, d, and the non-dimensional Bloch modes W, Θ_x , and Θ_y as

$$w(x, y, z, t) = W(x, y)\eta(t)d, \quad \theta_x(x, y, z, t) = \Theta_x(x, y)\eta(t)\frac{d}{a}, \quad \text{and} \quad \theta_y(x, y, z, t) = \Theta_y(x, y)\eta(t)\frac{d}{a}$$
(13)

Next, taking the amplitude of each equation in Eq. (13) (i.e., evaluating η , w, θ_x , and θ_y at the time that maximizes the sinusoidal function $\eta(t)$, denoted by $|\bullet|$) and solving for the non-dimensional Bloch modes yields the expressions:

$$W(x,y) = \frac{1}{d} |w(x,y,z,t)|, \quad \Theta_x(x,y) = \frac{a}{d} |\theta_x(x,y,z,t)|, \quad \text{and} \quad \Theta_y(x,y) = \frac{a}{d} |\theta_y(x,y,z,t)|$$
(14)

which can be employed to generate non-dimensional Bloch modes from a single FEEA and thus describe the vibration at the BG bound for any metamaterial unit cell of similar reference geometry. Substituting Eq. (13) into Eq. (12) and taking the amplitude of the resulting equation, this yields

$$= \frac{d^2}{24} \int_A \frac{Eh^3}{(1 - \nu^2)a^2} \left(\left(\frac{\partial \Theta_y}{\partial x} \right)^2 - 2\nu \frac{\partial \Theta_y}{\partial x} \frac{\partial \Theta_x}{\partial y} + \left(\frac{\partial \Theta_x}{\partial y} \right)^2 + \left(\frac{1 - \nu}{2} \right) \left(\frac{\partial \Theta_y}{\partial y} - \frac{\partial \Theta_x}{\partial x} \right)^2 \right) dA + \cdots$$

$$(15)$$

$$\cdots + \frac{d^2}{4} \int_A \frac{k_s Eh}{(1+\nu)} \left(\left(\frac{\partial W}{\partial x} + \frac{1}{a} \Theta_y \right)^2 + \left(\frac{\partial W}{\partial y} - \frac{1}{a} \Theta_x \right)^2 \right) dA$$

where v_{max} is defined to be the maximum (equivalent to amplitude for a scalar variable) potential energy in the vibrating unit cell.

Finally, consider changing variables from x and y defined over the planar area A used to generate the Bloch modes to $x' \equiv x/a$ and $y' \equiv y/a$ defined over a dimensionless planar area A' describing a general metamaterial of any unit cell size, and further, consider defining a non-dimensional thickness y by $y \equiv h/a$ to replace the element thicknesses h in Eq. (15). Substituting these into Eq. (15) yields

$$\mathcal{V}_{\text{max}} = \frac{d^2}{24} \int_{A'} \frac{E \gamma^3 a}{(1 - \nu^2)} \left(\left(\frac{\partial \Theta_y}{\partial x'} \right)^2 - 2\nu \frac{\partial \Theta_y}{\partial x'} \frac{\partial \Theta_x}{\partial y'} + \left(\frac{\partial \Theta_x}{\partial y'} \right)^2 + \left(\frac{1 - \nu}{2} \right) \left(\frac{\partial \Theta_y}{\partial y'} - \frac{\partial \Theta_x}{\partial x'} \right)^2 \right) dA' + \cdots \\
\cdots + \frac{d^2}{4} \int_{A'} \frac{k_s E \gamma a}{(1 + \nu)} \left(\left(\frac{\partial W}{\partial x'} + \Theta_y \right)^2 + \left(\frac{\partial W}{\partial y'} - \Theta_x \right)^2 \right) dA' \tag{16}$$

where the chain rule and the Jacobian of the transformation from A to A' were used to obtain this expression, giving the maximum potential energy of the vibrating unit cell as a function of the elastic modulus E and Poisson's ratio ν of the materials comprising the metamaterial, the non-dimensional thicknesses γ of the unit cell's constitutive elements, the non-dimensional Bloch modes W, Θ_x , and Θ_v , the characteristic length a, and the amplitude a of the unit cell's vibration.

3.2. Kinetic energy analysis

Using the Mindlin plate element shown in Fig. 3 defining the kinematic variables u, v, w, θ_x , and θ_y , we now aim to determine the maximum kinetic energy in the metamaterial unit cell of characteristic length a vibrating with amplitude d and non-dimensional Bloch modes W, Θ_x , and Θ_y . To do this, let the kinetic energy of the unit cell as a function of time be denoted by $\mathcal{T}(t)$ and defined as

$$\mathcal{T}(t) = \frac{1}{2} \int_{V} \rho \left(\dot{u}^{2} + \dot{v}^{2} + \dot{w}^{2} \right) dV = \frac{1}{2} \int_{V} \rho \left(\dot{w}^{2} + z^{2} \left(\dot{\theta}_{x}^{2} + \dot{\theta}_{y}^{2} \right) \right) dV \tag{17}$$

where Eq. (1) has been substituted to obtain the second equation and $\rho = \rho(x, y)$ is the mass density of the materials comprising the unit cell. Analogous to the method used for $\mathcal{V}(t)$ in Section 3.1, splitting this expression for $\mathcal{T}(t)$ into an integral over the mid-planar area of the plate A and an integral over the plate thickness z gives the relation:

$$\mathcal{T}(t) = \frac{1}{2} \int_{A} \rho \left(h \dot{w}^{2} + \frac{h^{3}}{12} \left(\dot{\theta}_{x}^{2} + \dot{\theta}_{y}^{2} \right) \right) dA \tag{18}$$

and taking the amplitude of the resulting equation yields

$$\mathcal{T}_{\text{max}} \equiv |\mathcal{T}(t)| = \frac{1}{2} \int_{A} \rho \left(h |\dot{w}|^{2} + \frac{h^{3}}{12} \left(|\dot{\theta}_{x}|^{2} + |\dot{\theta}_{y}|^{2} \right) \right) dA \tag{19}$$

where \mathcal{T}_{max} is the maximum kinetic energy in the vibrating unit cell. Using the assumption that w, θ_{x} , and θ_{y} each vary sinusoidally with time, the amplitudes $|\dot{w}|$, $|\dot{\theta}_{\text{x}}|$, and $|\dot{\theta}_{\text{y}}|$ can each be written in terms of the angular frequency ω as

$$|\dot{w}| = \omega |w|, \quad |\dot{\theta}_x| = \omega |\theta_x|, \quad \text{and} \quad |\dot{\theta}_y| = \omega |\theta_y|$$
 (20)

which can be substituted into Eq. (19) to give

$$\mathcal{T}_{\text{max}} \equiv |\mathcal{T}(t)| = \frac{\omega^2}{2} \int_A \rho \left(h |w|^2 + \frac{h^3}{12} \left(\left| \theta_{\text{x}} \right|^2 + \left| \theta_{\text{y}} \right|^2 \right) \right) dA \tag{21}$$

Finally, substituting Eq. (13) for w, θ_x , and θ_y , changing variables from x and y to the non-dimensional x' and y', and substituting for the non-dimensional thicknesses γ as in Section 3.1 yields

$$\mathcal{T}_{\text{max}} = \frac{d^2 \omega^2}{2} \int_{A'} \rho a^3 \left(\gamma W^2 + \frac{\gamma^3}{12} \left(\Theta_x^2 + \Theta_y^2 \right) \right) dA' \tag{22}$$

as an expression for the maximum kinetic energy in the vibrating unit cell as a function of the mass density ρ of the materials comprising the metamaterial, the non-dimensional thicknesses γ of the unit cell's constitutive elements, the non-dimensional Bloch modes W, Θ_x , and Θ_y , the characteristic length a, and the amplitude a of the unit cell's vibration.

3.3. Conservation of energy

Using the expressions for the maximum potential and kinetic energies in the vibrating unit cell in Eqs. (16) and (22), respectively, and assuming negligible material damping, a straightforward energy argument can now be presented for determining the vibration frequency that must accompany the motion defined by the non-dimensional Bloch modes W, Θ_x , and Θ_y , the unit cell geometry, and material properties. To do this, we first make note of the fact that either the potential or kinetic energies in the vibrating unit cell must be zero when the other quantity is maximized as a consequence of the assumed sinusoidal vibration of the unit cell. Therefore, both the maximum potential and kinetic energies derived in Eqs. (16) and (22) must be equivalent to the total energy in the unit cell. Treating the unit cell as a control volume, conservation of energy requires that:

$$\mathcal{E}(t)|_{\mathcal{V}_{\text{max}}} = (\mathcal{V}(t) + \mathcal{T}(t))|_{\mathcal{V}_{\text{max}}} = \mathcal{V}_{\text{max}} \text{ and } \mathcal{E}(t)|_{\mathcal{T}_{\text{max}}} = (\mathcal{V}(t) + \mathcal{T}(t))|_{\mathcal{T}_{\text{max}}} = \mathcal{T}_{\text{max}} \implies \mathcal{V}_{\text{max}} = \mathcal{T}_{\text{max}}$$
 (23)

where $\mathcal{E}(t)|_{\mathcal{V}_{\text{max}}} = \mathcal{E}(t)|_{\mathcal{T}_{\text{max}}} \equiv \mathcal{E}$ denotes the total conserved energy in the unit cell. Substituting Eq. (16) for \mathcal{V}_{max} and Eq. (22) for \mathcal{T}_{max} into Eq. (23) gives

$$\frac{d^{2}}{24} \int_{A'} \frac{E \gamma^{3} a}{(1 - \nu^{2})} \left(\left(\frac{\partial \Theta_{y}}{\partial x'} \right)^{2} - 2\nu \frac{\partial \Theta_{y}}{\partial x'} \frac{\partial \Theta_{x}}{\partial y'} + \left(\frac{\partial \Theta_{x}}{\partial y'} \right)^{2} + \left(\frac{1 - \nu}{2} \right) \left(\frac{\partial \Theta_{y}}{\partial y'} - \frac{\partial \Theta_{x}}{\partial x'} \right)^{2} \right) dA' + \cdots$$

$$\cdots + \frac{d^{2}}{4} \int_{A'} \frac{k_{s} E \gamma a}{(1 + \nu)} \left(\left(\frac{\partial W}{\partial x'} + \Theta_{y} \right)^{2} + \left(\frac{\partial W}{\partial y'} - \Theta_{x} \right)^{2} \right) dA'$$

$$= \frac{d^{2} \omega^{2}}{2} \int_{A'} \rho a^{3} \left(\gamma W^{2} + \frac{\gamma^{3}}{12} \left(\Theta_{x}^{2} + \Theta_{y}^{2} \right) \right) dA'$$
(24)

relating the angular frequency ω to the non-dimensional Bloch modes, material properties, and geometry of the H–S–H metamaterial unit cell.

To simplify the form of this equation, consider defining an equivalent bending stiffness K_b , an equivalent transverse shear stiffness K_s , and an equivalent mass M of the unit cell, respectively as

$$K_{b} \equiv \int_{A'} \frac{E \gamma^{3} a}{12(1 - \nu^{2})} \left(\left(\frac{\partial \Theta_{y}}{\partial x'} \right)^{2} - 2\nu \frac{\partial \Theta_{y}}{\partial x'} \frac{\partial \Theta_{x}}{\partial y'} + \left(\frac{\partial \Theta_{x}}{\partial y'} \right)^{2} + \left(\frac{1 - \nu}{2} \right) \left(\frac{\partial \Theta_{y}}{\partial y'} - \frac{\partial \Theta_{x}}{\partial x'} \right)^{2} \right) dA'$$
 (25)

$$K_{s} \equiv \int_{A'} \frac{k_{s} E \gamma a}{2(1+\nu)} \left(\left(\frac{\partial W}{\partial x'} + \Theta_{y} \right)^{2} + \left(\frac{\partial W}{\partial y'} - \Theta_{x} \right)^{2} \right) dA' \tag{26}$$

and

$$M \equiv \int_{A'} \rho a^3 \left(\gamma W^2 + \frac{\gamma^3}{12} \left(\Theta_x^2 + \Theta_y^2 \right) \right) dA' \tag{27}$$

Substituting these definitions into Eq. (24) reveals the following:

$$\frac{1}{2}d^2(K_b + K_s) = \frac{1}{2}Md^2\omega^2 \implies f = \frac{\omega}{2\pi} = \frac{1}{2\pi}\sqrt{\frac{K_b + K_s}{M}}$$
(28)

giving a concise expression for the vibration frequency f independent of the vibration amplitude and in terms of the stiffness and mass expressions K_b , K_s , and M, which are themselves defined as functions of the material properties E, ν , and ρ , the non-dimensional element thicknesses γ , the characteristic length a, the mid-planar geometry (defining A and A'), and the non-dimensional Bloch modes W, Θ_x , and Θ_y describing the vibration at the BG bound for all H–S–H metamaterials with the given reference geometry.

Wave Motion 105 (2021) 102734

Eqs. (25) through (28) provide a pragmatic technique for calculating the vibration frequency of *any H–S–H metamaterial* of specific reference geometry—and hence, the limits of the first frequency BG—from its non-dimensional Bloch modes computed with a *single* FEEA. However, it is critical to note that this approach relies on accurate computation of both the spatial derivatives and integrals of the Bloch modes in Eqs. (25) through (27), an endeavor that can be cumbersome—if not impossible—to achieve directly with finite element data. Motivated by this difficulty, a system identification analysis of these non-dimensional Bloch modes is next considered to establish continuous surface equations from finite element data which can be directly employed by symbolic or numerical calculus in the preceding equations, therefore providing *algebraic expressions* for the limits of the first transverse frequency BG of any similar metamaterial in terms of precomputed integrals involving the continuously-known non-dimensional Bloch modes. A technique for conducting this identification is presented in the following section.

4. System identification of Bloch mode shapes

In this section, we provide observations of symmetry in H–S–H metamaterials (Section 4.1) and a Least Squares Identification Model (Section 4.2) for identifying surface equations for a given set of unit cell Bloch modes determined by FEEA, using the simple yet prevailing case of H–S–H metamaterials with square filler and resonator elements as the archetypal geometry. The overarching objective is to introduce a technique for computing the integral equations for the stiffness and mass values in Eqs. (25) through (27) and thus provide a novel procedure for computing the first transverse frequency BG of *any metamaterial* of similar reference geometry with a single finite element eigenfrequency analysis. Following this presentation, Sections 5 and 6 will apply this procedure to sample metamaterials to illustrate the powerful computational promise and insights of this methodology.

4.1. Observing symmetry in H–S–H Bloch modes

As demonstrated earlier, in H–S–H metamaterials with sufficiently soft filler material, the displacement and rotation Bloch modes at the limits of the first transverse frequency BG are observed to attain the same non-dimensional mode shapes across all metamaterials of similar reference geometry. Using the technique detailed in the following section, continuous surface equations for each of the non-dimensional Bloch modes W, Θ_x , and Θ_y can be computed, which can be substituted into Eqs. (25) through (28) to determine the BG frequencies. However, two further observations of symmetry in these Bloch modes at the limits of the first BG can be made to significantly reduce the number of required identification analyses in this procedure. The first is between the Bloch modes at the lower and upper limits of the first BG, and the second is between the x- and y-rotation modes at a single BG bound—both of which significantly simplify the identification procedure.

It can be observed that both the displacement and rotational Bloch modes at the upper bound of the first BG can be approximated by the same surface equations as the Bloch modes at the lower bound, leading to the conclusion that only the lower bound Bloch modes need to be included in the identification analysis. To illustrate this observation, Fig. 4 displays the non-dimensional Bloch modes W, Θ_x , and Θ_y at the lower and upper limits of the first BG for the H-S-H unit cell analyzed in Section 2. Upon inspection of these surface plots, it can be observed that the x-rotation Bloch mode at the upper bound of the BG has nearly the same mode shape as the x-rotation mode at the lower bound (Figs. 4b and e), the y-rotation mode at the upper bound has nearly the same mode shape as the y-rotation mode at the lower bound (Figs. 4c and f), and the displacement mode at the upper bound has nearly the same mode shape as the displacement mode at the lower bound, with a constant shift equal to the center of mass of the lower bound displacement mode subtracted from the lower bound mode shape to obtain the mode shape at the upper bound (Figs. 4a and d; Section 2). Although it is impossible to quantify the error between these mode shapes for every conceivable unit cell configuration, the errors for this particular unit cell and for all cases studied do not exceed 6% of the displacement amplitude for the displacement mode shape and 2.5% of the rotation amplitude for the rotation mode shapes, with average absolute errors in finite element data between the exact and approximated upper bound modes less than 2% and 0.5% for the displacement and rotation modes, respectively. These small errors will be readdressed in Section 5 where it will be shown that they can be neglected in the identification analysis, enabling us to determine both bounds of the BG in the identification procedure with the lower bound Bloch modes only and without significant error.

As a second observation, we note that the *y*-rotation Bloch mode at the lower or upper bound of the first BG can be obtained from the *x*-rotation mode at the same bound with exact accuracy for rotationally-symmetric unit cells, where "rotationally-symmetric" denotes a geometry that does not change when rotated by 90° in either direction about the *z*-axis. This is demonstrated for the current set of Bloch modes in Fig. 4, which shows that the surface equation for the *y*-rotation Bloch mode at either bound of the BG can be obtained from that of the *x*-rotation Bloch mode at the same bound by a simple 90° counter-clockwise rotation about the *z*-axis. A closer inspection reveals that this hypothesis holds with exact accuracy, since rotational symmetry implies that the unit cell geometry is immutable to a 90° rotation about the *z*-axis, the definitions of θ_x and θ_y imply that any value of θ_x will be mapped to the same value of θ_y by a 90° rotation about the *z*-axis (Fig. 3), and such a rotation applied to a wavenumber pair at either the lower bound (M, $(\tilde{k}_x = \pi, \tilde{k}_y = \pi)$) or the upper bound (Γ , $(\tilde{k}_x = 0, \tilde{k}_y = 0)$) of the first BG will result in the same wavenumber pair after the rotation. (At M, $(\tilde{k}_x = \pi, \tilde{k}_y = \pi)$ will be mapped to $(\tilde{k}_x = \pi, \tilde{k}_y = \pi)$ by such a rotation, which is equivalent to $(\tilde{k}_x = \pi, \tilde{k}_y = \pi)$

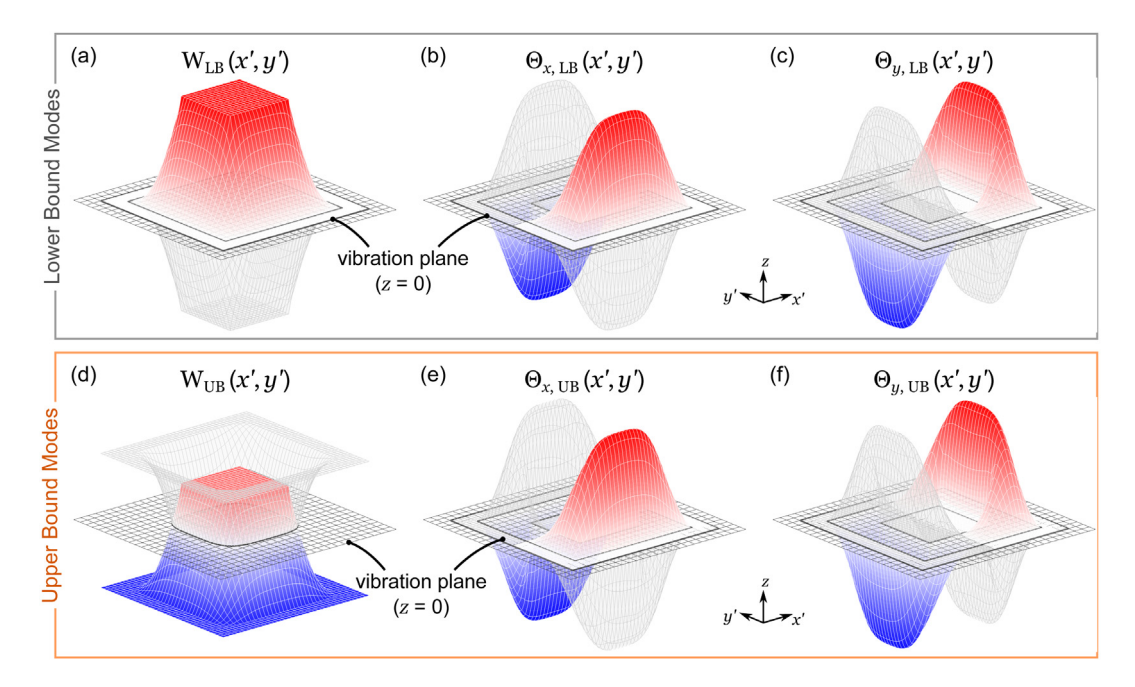


Fig. 4. Non-dimensional displacement and rotation Bloch mode shapes at the lower and upper bounds of the first BG for an H–S–H metamaterial with 90° rotational symmetry and rectangular filler and resonator elements, determined from FEEA: (a) lower bound W, (b) lower bound Θ_x , (c) lower bound Θ_y , (d) upper bound W, (e) upper bound Θ_x , and (f) upper bound Θ_y .

due to the 2π -periodic nature of the Brillouin zone). As a result of this, for the archetypal case of H–S–H unit cells with rotational symmetry, the *y*-rotation modes do not need to be determined by an identification procedure.

Finally, it can be observed that due to the natural design of H–S–H metamaterials with soft filler material, the matrix and resonator elements do not deform and only the filler component attains significant deformation—this is the defining feature of H–S–H metamaterials leading to the fact that all H–S–H metamaterials with specific reference geometry share the same Bloch modes at both bounds of the first BG. Applying this to the previous observations, we conclude that only the lower bound displacement and *x*-rotation Bloch modes of the filler material of an H–S–H unit cell need to be identified for the entire mode shapes at both the lower and upper BG bounds to be determined, with the lower bound *y*-rotation Bloch mode of the filler material added to this list when the H–S–H unit cell does not contain rotational symmetry.

4.2. System identification procedure

Using the aforementioned symmetries, we propose a *Least Squares Identification Model* to compute continuous surface equations for an H–S–H unit cell using the minimum number of identification analyses, which can be employed to compute the first BG of any H–S–H metamaterials of similar reference geometry using the results of Section 3. We begin by partitioning the unit cell into areas of identification along the material boundaries and along sections of symmetry in the unit cell, exemplified for the rotationally-symmetric H–S–H unit cell with square filler and resonator elements discussed to this point in the paper. Following this, we provide a mathematical foundation for the identification algorithm, formulate and solve the least squares analysis for the appropriate Bloch mode sections, and simplify computations for partitioned sections expressed by finite element data on a rectangular grid of data points. A slightly generalized identification algorithm to be used when such a rectangular grid of data points on a partitioned section is not available is then presented and a method for quantifying error in the identification algorithm is established.

4.2.1. Partitioning unit cell Bloch modes

Making use of symmetries in the filler region of the Bloch modes apparent in Fig. 4, consider the partition of the lower bound displacement and x-rotation Bloch modes of this sample unit cell shown in Fig. 5, using lines extending from the corners of the square resonator parallel to the sides of the unit cell and intersecting the boundary between the filler and matrix elements to generate the partition. Let us define the section of the displacement mode in the third quadrant of the unit cell by W_{corner} , shown as a section of the complete displacement mode in non-dimensional (x', y') coordinates and over a transformed, isoparametric region in (r, s) coordinates in Figs. 5a and c, respectively. This and all other non-dimensional Bloch mode sections to be identified by least squares analyses are transformed to the (r, s) region for consistency in the least squares procedure and to ensure that each mode section is defined over a rectangular region (this latter reason will be evident in the following section), in which $-1 \le r, s \le 1$. Notice from symmetry of the

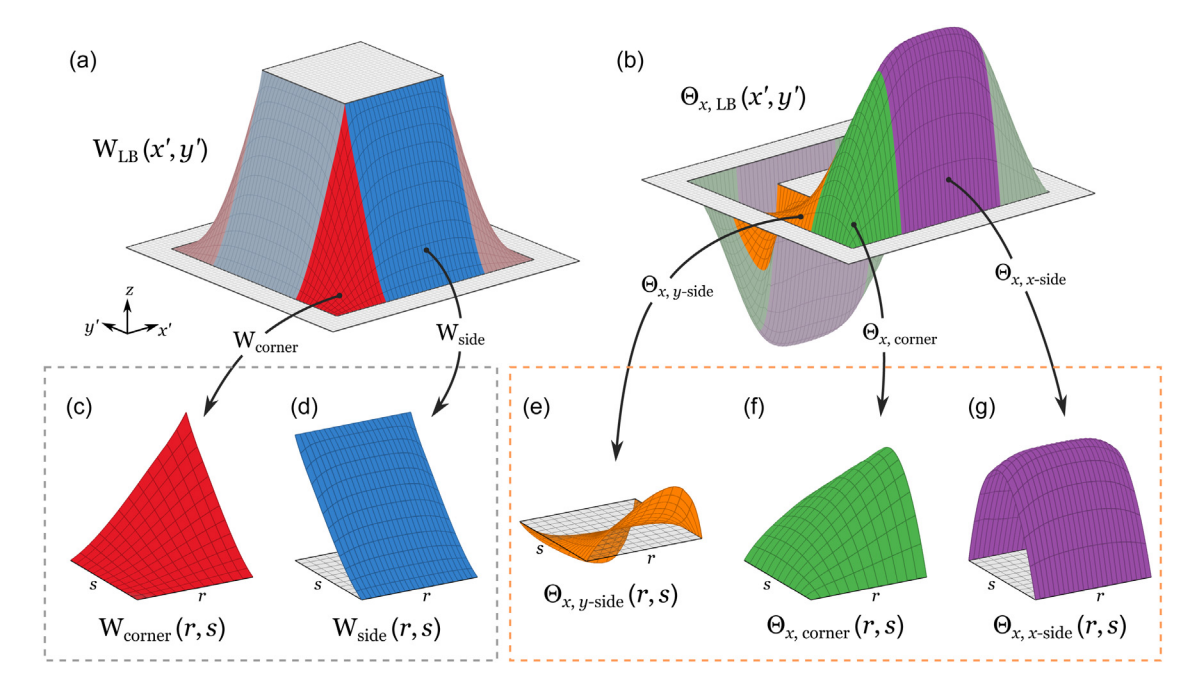


Fig. 5. System identification partition for a sample H–S–H unit cell for non-dimensional (a) displacement and (b) x-rotation Bloch mode shapes. Off-white colors represent rigid sections (matrix and resonator). Red and blue colors represent the corner and side sections of the displacement mode, respectively. Orange, green, and violet colors represent the y-side, corner, and x-side sections of the x-rotation mode, respectively. Muted colors represent repeated sections of the filler material. (c) through (g) display the transformed Bloch mode shape sections W_{corner} , W_{side} , Θ_{x,y -side}, $\Theta_{x,x}$ -side over the planar area (r,s) that uniquely define the sections requiring identification. (For interpretation of the references to color in this figure legend, the reader is referred to the web version of this article.)

displacement mode that the W_{corner} mode shape is repeated three times over the remaining filler sections of the Bloch mode—sections that can therefore be eliminated from the identification procedure. Similarly, let us define the section of the displacement mode spanning the third and fourth quadrants of the unit cell by W_{side} , shown in Figs. 5a and d and again repeated three times in the remainder of the Bloch mode. Together, W_{corner} and W_{side} capture all unique sections of the displacement Bloch mode requiring identification.

Analogous to the displacement Bloch mode, consider a similar partition of the x-rotation Bloch mode shown in Fig. 5b, where $\Theta_{x,corner}$ defines the filler section in the third quadrant of the unit cell, $\Theta_{x,x-side}$ defines the filler section spanning the third and fourth quadrants, and $\Theta_{x,y-side}$ defines the filler section spanning the second and third quadrants of the unit cell, shown as combined sections in Fig. 5b and over isoparametric regions in Figs. 5f, g, and e, respectively. Notice that three, rather than two, unique sections of the partition are required here due to a lack of symmetry about the xz-plane for this x-rotation mode. Together, W_{corner} , W_{side} , $\Theta_{x,corner}$, $\Theta_{x,x-side}$, and $\Theta_{x,y-side}$ transformed to (r,s) coordinates provide unique isoparametric sections on which to conduct piecewise identification analyses for any H–S–H metamaterial with rotationally symmetric unit cells and square filler and resonator elements. Finally, while this specific metamaterial and partition are applied in the remainder of this paper, we note that a similar partition can be generated for other H–S–H geometries employing non-square, non-symmetric, and non-rectangular elements, with different transformations from the non-rectangular mode sections to isoparametric regions required in these scenarios.

4.2.2. Mathematical foundations

Consider a specific partition of the non-dimensional Bloch modes W, Θ_x , and Θ_y for an H–S–H unit cell, and consider a specific section of that partition for either the displacement or rotation Bloch modes denoted by S. Further suppose that the region of the unit cell defined by S is transformed from the region (x', y') to the isoparametric region (r, s) as illustrated in Fig. 5 (with $-1 \le r, s \le 1$) and that values of S(r, s) have been determined by FEEA on a set of discrete data points over the isoparametric region. Finally, suppose that linearly independent basis functions $f_i(r)$ and $g_j(s)$ are chosen separately in the r- and s-directions (where $1 \le i \le m$ and $1 \le j \le n$) to capture surface equations for S(r, s) over the isoparametric region. (Our reason for choosing separate basis functions in the r- and s-directions will be revealed shortly). The objective of the remainder of the system identification procedure is to determine the best-fit surface equation to the discrete FEEA data using the chosen basis functions as the general shape of the isoparametrically-defined Bloch mode section.

Suppose that f(r) and g(s) are $m \times 1$ and $n \times 1$ column vectors containing the independent basis functions $f_i(r)$ and $g_i(s)$, respectively. That is:

$$\mathbf{f}(r) \equiv \begin{bmatrix} f_1(r) & \cdots & f_m(r) \end{bmatrix}^{\mathsf{T}} \quad \text{and} \quad \mathbf{g}(s) \equiv \begin{bmatrix} g_1(s) & \cdots & g_n(s) \end{bmatrix}^{\mathsf{T}}$$
 (29)

Using this set of basis functions, an expression for the values of the mode section over the isoparametric region as a continuous equation can be written as

$$S(r,s) = \mathbf{f}(r)^{\mathrm{T}} C \mathbf{g}(s) \tag{30}$$

where C is an $m \times n$ matrix of constants. In this section through Section 4.2.4, it will be assumed that the known mode section data computed by FEEA and transformed to the isoparametric region are expressed on a *rectangular grid* of data points, with Section 4.2.5 providing an alternative solution when the data for the mode section are not expressed in this rectangular format. In both formats of the known data, the optimal surface equation for S(r,s) in the form of Eq. (30) is defined to be the solution with the precise values of C that give a least squares agreement between the finite element data and the values of the identified solution evaluated at those data points.

If the finite element data are known on a rectangular grid of data points, suppose that this grid is represented by a vector of r-values of length p ($\mathbf{r} = [r_1 \cdots r_p]^T$) and a vector of s-values of length q ($\mathbf{s} = [s_1 \cdots s_q]^T$), for which any two values (r_i, s_j) with $1 \le i \le p$ and $1 \le j \le q$ form the (r, s) coordinates of a single data point. Now suppose that the known (FEEA) value of the Bloch mode section at the point (r_i, s_j) is denoted by $\tilde{S}(r_i, s_j)$, and that the least squares estimate of this value calculated with the representation of Eq. (30) is denoted by $\hat{S}(r_i, s_j)$. The value of the mode section at the point (r_i, s_j) computed from the identified representation can therefore be expressed as

$$\hat{\mathbf{S}}(r_i, s_i) = \mathbf{f}(r_i)^{\mathrm{T}} \mathbf{C} \mathbf{g}(s_i) \tag{31}$$

which in expanded matrix form can be written as

$$\hat{S}(r_i, s_j) = \begin{bmatrix} f_1(r_i) & \cdots & f_m(r_i) \end{bmatrix} \begin{bmatrix} C_{1,1} & \cdots & C_{1,n} \\ \vdots & \ddots & \vdots \\ C_{m,1} & \cdots & C_{m,n} \end{bmatrix} \begin{bmatrix} g_1(s_j) \\ \vdots \\ g_n(s_j) \end{bmatrix}$$
(32)

with the middle matrix expression of the RHS of Eq. (32) denoting the values of the matrix C. Expanding and regrouping terms in this equation, Eq. (32) can be written as

$$\hat{S}(r_i, s_i) = A_{i,i} \mathbf{c} \tag{33}$$

where

$$A_{i,j} \equiv \begin{bmatrix} f_1(r_i)g_1(s_j) & \cdots & f_1(r_i)g_n(s_j) & | & \cdots & | & f_m(r_i)g_1(s_j) & \cdots & f_m(r_i)g_n(s_j) \end{bmatrix}$$

$$(34)$$

is a $1 \times mn$ row vector, and

$$\mathbf{c} \equiv \begin{bmatrix} C_{1,1} & \cdots & C_{1,n} & \cdots & C_{m,1} & \cdots & C_{m,n} \end{bmatrix}^{\mathrm{T}}$$
(35)

is an $mn \times 1$ column vector containing reshaped values of C. Now consider expressing the values for each $\hat{\mathbf{S}}(r_i, s_j)$ in a similar manner to the way in which C was reshaped in the previous equation. That is, let the $pq \times 1$ vector $\hat{\mathbf{S}}(\boldsymbol{r}, \boldsymbol{s})$ be defined as

$$\hat{\mathbf{s}}(\mathbf{r},\mathbf{s}) \equiv \begin{bmatrix} \hat{\mathbf{S}}(r_1,s_1) & \cdots & \hat{\mathbf{S}}(r_1,s_q) & | & \cdots & | & \hat{\mathbf{S}}(r_p,s_1) & \cdots & \hat{\mathbf{S}}(r_p,s_q) \end{bmatrix}^{\mathrm{T}}$$
(36)

containing values of the identified solution at each of the pq data points in the isoparametric region. Similarly, let the data in each value of $\tilde{S}(r_i, s_j)$ be expressed in a $pq \times 1$ column vector $\tilde{s}(r, s)$ containing the pq values of S determined from FEEA, defined as

$$\tilde{\mathbf{s}}(\mathbf{r},\mathbf{s}) \equiv \begin{bmatrix} \tilde{\mathbf{S}}(r_1,s_1) & \cdots & \tilde{\mathbf{S}}(r_1,s_q) & | & \cdots & | & \tilde{\mathbf{S}}(r_p,s_1) & \cdots & \tilde{\mathbf{S}}(r_p,s_q) \end{bmatrix}^{\mathrm{T}}$$
(37)

Finally, substituting the simplified expression for $\hat{S}(r_i, s_j)$ from Eq. (33) into Eq. (36) yields the equation:

$$\hat{\mathbf{s}}(\mathbf{r},\mathbf{s}) = \begin{bmatrix} A_{1,1}^{\mathsf{T}} & \cdots & A_{1,q}^{\mathsf{T}} & \cdots & A_{p,1}^{\mathsf{T}} & \cdots & A_{p,q}^{\mathsf{T}} \end{bmatrix}^{\mathsf{T}} \mathbf{c} = A\mathbf{c}$$
(38)

where A is the $pq \times mn$ matrix defined by

$$A \equiv \begin{bmatrix} A_{1,1}^{\mathsf{T}} & \cdots & A_{1,q}^{\mathsf{T}} & | & \cdots & | & A_{p,1}^{\mathsf{T}} & \cdots & A_{p,q}^{\mathsf{T}} \end{bmatrix}^{\mathsf{T}}$$

$$(39)$$

Eqs. (36) and (37) describing the estimates and measured values for the transformed Bloch mode section, the basis function vectors $\mathbf{f}(r)$ and $\mathbf{g}(s)$ in Eqs. (29) and (30) describing the general representation of the identified solution, and Eqs. (34) and (39) defining the matrix of basis function evaluations A are all that are needed to conduct the least squares analysis fitting the finite element data to the surface equation representation for the given Bloch mode section, as will be detailed next.

4.2.3. Least squares solution

The objective of the least squares analysis is to identify the coefficients \mathbf{c} in Eq. (35) that give the optimal surface equation for the data $\tilde{S}(r,s)$ using the basis function representation in Eq. (30). Here, "optimal" is defined as optimality in the least squares sense, for which the sum of the squares of the errors between the finite element values $\tilde{S}(r_i,s_j)$ and the identified values $\hat{S}(r_i,s_j)$ attains its minimum value. Mathematically, employing the vector representations of \hat{S} and \hat{S} in Eqs. (36) and (37) and the expression for $\hat{\mathbf{s}}(\mathbf{r},\mathbf{s})$ in Eq. (38), this definition of optimality requires minimization of the following cost function:

$$J = \sum_{i=1}^{p} \sum_{i=1}^{q} \left(\tilde{\mathbf{s}}(r_i, s_j) - \hat{\mathbf{s}}(r_i, s_j) \right)^2 = \left(\tilde{\mathbf{s}} - \hat{\mathbf{s}} \right)^{\mathsf{T}} \left(\tilde{\mathbf{s}} - \hat{\mathbf{s}} \right) = \left(\tilde{\mathbf{s}} - A \mathbf{c} \right)^{\mathsf{T}} \left(\tilde{\mathbf{s}} - A \mathbf{c} \right)$$
(40)

which has the well-established solution [26]:

$$\mathbf{c} = (A^{\mathsf{T}}A)^{-1}A^{\mathsf{T}}\,\tilde{\mathbf{s}}\tag{41}$$

Such a solution for c in Eq. (41) is uniquely defined when the number of rows of A (pq) equals or exceeds the number of columns of A (mn), or equivalently, when there is sufficient finite element data such that there is at least one finite element data point for every combination of basis functions in f(r) and g(s). This simply indicates that the product of the number of basis functions in the r- and s-directions (mn) must not exceed the amount of available finite element data (pq), or more strongly, that both $m \le p$ and $n \le q$ must hold as explained in the following section. Using Eq. (41) for the column vector c, the values of c can be reshaped into the matrix c by inversion of Eq. (35) and substituted into the representation of Eq. (30) to give a continuous surface equation for the Bloch mode section c0 defined by the FEEA data and the basis functions vectors c1 and c2. This continuous equation for the mode section can then be transformed to c3. This coordinates along with the remaining partitioned sections to yield a complete piecewise representation of the non-dimensional Bloch modes using continuous surface equations.

4.2.4. Kronecker factorization

While the surface equations for each mode section computed with Eqs. (29) through (41) could now be substituted directly into Eqs. (25) through (28) to determine the frequency bounds of the first BG, such a solution relies on inversion of the A^TA matrix of size $mn \times mn$ (Eq. (41)), which may become computationally expensive to evaluate as the number of basis functions increases. In this section, a simple yet efficient algorithm achievable for a rectangular grid of data points is presented which provides an equivalent evaluation for the constant vector \mathbf{c} , minimizes the size of the matrix inversion in the computation, and significantly reduces the computational expense required for the analysis. When the FEEA data transformed to the (r, s) region can be expressed on a rectangular grid of data points, it can be shown that the matrix of basis function evaluations A defined in Eqs. (34) and (39) can be expressed as

$$A = A_r \otimes A_s \tag{42}$$

where A_r and A_s are defined as

$$A_{r} \equiv \begin{bmatrix} f_{1}(r_{1}) & \cdots & f_{m}(r_{1}) \\ \vdots & \ddots & \vdots \\ f_{1}(r_{p}) & \cdots & f_{m}(r_{p}) \end{bmatrix} \text{ and } A_{s} \equiv \begin{bmatrix} g_{1}(s_{1}) & \cdots & g_{n}(s_{1}) \\ \vdots & \ddots & \vdots \\ g_{1}(s_{q}) & \cdots & g_{n}(s_{q}) \end{bmatrix}$$

$$(43)$$

and $A_r \otimes A_s$ denotes the Kronecker product of A_r and A_s . Substituting this factored expression for A into Eq. (41) and using properties of the Kronecker product shown in [26], the least squares solution for c simplifies to

$$\mathbf{c} = (A_{IS,r} \otimes A_{IS,s})\,\tilde{\mathbf{s}}\tag{44}$$

where $A_{LS,r}$ and $A_{LS,s}$ are separate least squares solution matrices, defined by

$$A_{LS,r} \equiv \left(A_r^{\mathsf{T}} A_r\right)^{-1} A_r^{\mathsf{T}} \text{ and } A_{LS,s} \equiv \left(A_s^{\mathsf{T}} A_s\right)^{-1} A_s^{\mathsf{T}}$$

$$(45)$$

of size $m \times p$ and $n \times q$ respectively.

Recall from Section 4.2.2 that the matrix A has size $pq \times mn$ in the least squares analysis, leading to the inverse of an $mn \times mn$ matrix in Eq. (41) required in the direct computation of Section 4.2.3. On the other hand, the equivalent solution employing the Kronecker factorization in Eqs. (44) and (45) reduces the computation from a single inversion of an $mn \times mn$ matrix to smaller inversions of $m \times m$ ($A_r^T A_r$) and $n \times n$ ($A_s^T A_s$) matrices, along with a computationally-efficient Kronecker product of the solutions $A_{LS,r}$ and $A_{LS,s}$. Such a factorization for data expressed on a rectangular grid of data points is achievable as long as the number of basis functions does not exceed the length of the data grid in the r- or s-directions ($m \le p$ and $n \le q$, respectively) to ensure that $A_r^T A_r$ and $A_s^T A_s$ in Eq. (45) are both invertible matrices. Since the Kronecker product is a fast computation relative to matrix inversion, this factorization when possible reduces the speed of the least squares computation from $\mathcal{O}^{n_{\text{inv}}}$ to $\mathcal{O}^{n_{\text{inv}}}$, where $\mathcal{O}^{n_{\text{inv}}}$ is the algorithmic efficiency of the procedure used to calculate the $\left(A_r^T A_r\right)^{-1}$ and $\left(A_s^T A_s\right)^{-1}$ matrix inverses in Eq. (45).

4.2.5. Non-rectangular identification procedure

In the identification regions of some H–S–H metamaterial unit cells, it may become difficult or unreasonable to express the finite element data for a Bloch mode section on a rectangular grid—in this scenario, a modified identification procedure can be followed that does not make use of the Kronecker factorization. The transformation of the identification section from the region (x', y') to the isoparametric region (r, s) is still required; however, the modified procedure can be applied to any distribution of data points over the region (r, s) albeit with reduced computational efficiency. Here, slightly modified equations to those in Sections 4.2.2 and 4.2.3 are presented that can be used to produce a continuous surface equation for such a mode section.

Instead of a rectangular grid of data points over the isoparametric region, suppose that the data have a general distribution of coordinates denoted by (r_k, s_k) , where $1 \le k \le l$ and l denotes the total number of data points in the mode section. Given this, let f(k) and g(k) denote the basis function vectors f(r) and g(s) representing the form of the mode section evaluated at index k. That is:

$$\mathbf{f}(r_k) = \begin{bmatrix} f_1(r_k) & \cdots & f_m(r_k) \end{bmatrix}^{\mathrm{T}} \text{ and } \mathbf{g}(s_k) = \begin{bmatrix} g_1(s_k) & \cdots & g_n(s_k) \end{bmatrix}^{\mathrm{T}}$$

$$(46)$$

And let

$$\hat{\mathbf{S}}(r_k, s_k) = \mathbf{f}(r_k)^{\mathrm{T}} \mathbf{C} \mathbf{g}(s_k) \tag{47}$$

denote the value of the mode section at the point (r_k, s_k) computed from the identified representation, using the same $m \times n$ matrix C defined in the previous analysis. Similar to Eqs. (36) and (37), let the values of the identified and FEEA solutions $\hat{S}(r_k, s_k)$ and $\tilde{S}(r_k, s_k)$ be respectively expressed as

$$\hat{\mathbf{s}}(\mathbf{r}_l, \mathbf{s}_l) \equiv \begin{bmatrix} \hat{\mathbf{S}}(r_1, s_1) & \cdots & \hat{\mathbf{S}}(r_l, s_l) \end{bmatrix}^{\mathrm{T}}$$
(48a)

$$\tilde{\mathbf{s}}(\mathbf{r}_l, \mathbf{s}_l) \equiv \left[\tilde{\mathbf{S}}(r_1, s_1) \quad \cdots \quad \tilde{\mathbf{S}}(r_l, s_l)\right]^{\mathrm{T}} \tag{48b}$$

where $\mathbf{r}_l \equiv [r_1 \cdots r_l]^{\mathrm{T}}$ and $\mathbf{s}_l \equiv [s_1 \cdots s_l]^{\mathrm{T}}$ contain the r- and s-values of each data point. Next, substituting Eq. (46) into Eq. (47) and expanding the result in a similar manner to Section 4.2.2 yields the equation:

$$\hat{S}(r_k, s_k) = (f_1(r_k)C_{1,1}g_1(s_k) + \dots + f_1(r_k)C_{1,n}g_n(s_k)) + \dots + (f_m(r_k)C_{m,1}g_1(s_k) + \dots + f_m(r_k)C_{m,n}g_n(s_k)) = B_k \mathbf{c}$$
(49)

where c is the $mn \times 1$ column vector defined in Eq. (35) and B_k is the following $1 \times mn$ row vector:

$$B_k \equiv \left[f_1(r_k)g_1(s_k) \cdots f_1(r_k)g_n(s_k) \right] \cdots \left[f_m(r_k)g_1(s_k) \cdots f_m(r_k)g_n(s_k) \right]$$

$$(50)$$

defined similarly to $A_{i,i}$ in Eq. (34). Substituting Eq. (49) into Eq. (48a) then yields the relations:

$$\hat{\mathbf{s}}(\mathbf{r}_l, \mathbf{s}_l) = \begin{bmatrix} B_1^{\mathsf{T}} & \cdots & B_l^{\mathsf{T}} \end{bmatrix}^{\mathsf{T}} \mathbf{c} = B\mathbf{c}$$
 (51)

where *B* is the following $l \times mn$ matrix:

$$B \equiv \begin{bmatrix} B_1^{\mathsf{T}} & \cdots & B_l^{\mathsf{T}} \end{bmatrix}^{\mathsf{T}} \tag{52}$$

containing information about the basis function vectors $\mathbf{f}(r_k)$ and $\mathbf{g}(s_k)$ evaluated at each of the l data points in the identification region.

Similar to the cost function defined in Eq. (40), the modified cost function expressing the sum of the squares of the errors between the FEEA data $\tilde{S}(r_k, s_k)$ and the identified values $\hat{S}(r_k, s_k)$ can then be written as

$$J' \equiv \sum_{k=1}^{L} \lambda_k \left(\tilde{\mathbf{s}}(r_k, s_k) - \hat{\mathbf{s}}(r_k, s_k) \right)^2 = \left(\tilde{\mathbf{s}} - \hat{\mathbf{s}} \right)^{\mathrm{T}} \Lambda \left(\tilde{\mathbf{s}} - \hat{\mathbf{s}} \right) = \left(\tilde{\mathbf{s}} - B\mathbf{c} \right)^{\mathrm{T}} \Lambda \left(\tilde{\mathbf{s}} - B\mathbf{c} \right)$$
(53)

where λ_k is an optional weighting parameter that may be introduced due to potential non-uniformity of the finite element points in the non-rectangular region (e.g., equivalent to the mesh density of the finite element nodes at each data point) and $\Lambda \equiv \operatorname{diag}(\lambda_1 \cdots \lambda_l)$ is an $l \times l$ diagonal matrix containing the weighting information (equal to the $l \times l$ identity matrix if weights are not used). Eq. (53) defines the new cost function needed to be minimized to determine the least squares coefficients in the optimal surface equation and has the solution [26]:

$$\mathbf{c} = \left(B^{\mathsf{T}} \Lambda B\right)^{-1} B^{\mathsf{T}} \Lambda \,\tilde{\mathbf{s}} \tag{54}$$

when the number of rows of B(l) equals or exceeds the number of columns of B(mn), or equivalently, when there are at least as many finite element data points for every combination of basis functions in f(r) and g(s), as in the previous analysis.

Finally, the vector c determined from this procedure can be reshaped into the matrix C using Eq. (35) and substituted into the basis function representation of Eq. (46) to give a continuous surface equation for the Bloch mode section S without requiring a rectangular grid of data points. However, when such a non-rectangular data distribution is present for the mode section, a general Kronecker factorization to simplify the computation does not exist—therefore, this version of the identification procedure relies on a direct inversion of the $mn \times mn$ matrix $B^T \Lambda B$ (Eq. (54)), yielding reduced computational efficiency but still a viable algorithm for most computational solvers.

4.2.6. Error auantification

To verify the accuracy of this system identification procedure, a quantifiable comparison between the identified mode section values \hat{S} (or \hat{s}) and the FEEA values \tilde{S} (or \tilde{s}) must be made in both identification procedures before using the resulting surface equations to determine metamaterial BGs. For the general case of any distribution of data points over the identification region, there exist l FEEA data points weighted by the $l \times l$ matrix Λ when conducting the least squares analysis, for which the weighted RMS error E_{rms} between the identified and FEEA values can be calculated as

$$E_{\text{rms}} \equiv \left(\frac{1}{\text{tr}(\Lambda)} \sum_{k=1}^{l} \lambda_k \left(\tilde{\mathbf{s}}(k) - \hat{\mathbf{s}}(k)\right)^2\right)^{1/2} = \left(\frac{1}{\text{tr}(\Lambda)} \left(\tilde{\mathbf{s}} - \hat{\mathbf{s}}\right)^T \Lambda \left(\tilde{\mathbf{s}} - \hat{\mathbf{s}}\right)\right)^{1/2}$$
(55)

and the average absolute error E_{avg} between each data point can be calculated as

$$E_{\text{avg}} \equiv \frac{1}{\text{tr}(\Lambda)} \sum_{k=1}^{l} \lambda_k \left| \tilde{\mathbf{s}}(k) - \hat{\mathbf{s}}(k) \right| \tag{56}$$

where $tr(\bullet)$ denotes the trace operator. Further, for sections of the unit cell partition for which rectangular data grids are present, the weighting matrix is identity and there exist pq data points in the identification region, leading to the expressions:

$$E_{\text{rms}} = \sqrt{\frac{1}{pq} \left(\tilde{\mathbf{s}} - \hat{\mathbf{s}} \right)^{\text{T}} \left(\tilde{\mathbf{s}} - \hat{\mathbf{s}} \right)} \text{ and } E_{\text{avg}} \equiv \frac{1}{pq} \sum_{i=1}^{p} \sum_{j=1}^{q} \left| \tilde{\mathbf{s}}(r_i, s_j) - \hat{\mathbf{s}}(r_i, s_j) \right|$$

$$(57)$$

for the RMS and average absolute error between the identified and FEEA solutions, respectively. Either representation of the identification error can be used to quantify the accuracy of the identified mode section and provide a quantifiable criterion for adding more or fewer basis functions to the vectors $\mathbf{f}(r)$ and $\mathbf{g}(s)$ employed in the analysis. Once surface equations are identified for each required section in the unit cell partition, these surface equations can be substituted into Eqs. (25) through (28) along with the characteristic length, element thicknesses, and material properties of the unit cell to determine the range of the first transverse frequency BG by this novel computation method.

4.3. Computing BGs using identified Bloch modes

At the conclusion of Section 3, it was claimed that the integrals involving W, Θ_x , and Θ_y in Eqs. (25) through (27) required to compute the first BG could be *pre-computed* using the identified Bloch modes after the system identification procedure, thus providing *algebraic expressions* for the first BG bounds of any H–S–H metamaterial of similar reference geometry to the one used to determine the non-dimensional Bloch modes. Here, we illustrate how those integrals can be employed to create an efficient algebraic expression for practically instantaneous computation of the first BG of H–S–H metamaterials.

Consider the definitions of bending stiffness K_b , shear stiffness K_s , and mass M of the unit cell in Eqs. (25) through (27), and suppose that i represents the ith section of the unit cell partition (i = 1, ..., N). If $W_{LB,i}$, $\Theta_{x,LB,i}$, and $\Theta_{y,LB,i}$ are used to denote the identified displacement, x-rotation, and y-rotation Bloch modes at the lower bound of the BG for the ith section of the unit cell, then the stiffness and mass values for this section can be expressed using the equations of Section 3 as

$$K_{b,LB,i} = \frac{E_{i}\gamma_{i}^{3}a}{12(1-\nu_{i}^{2})} \left(\int_{A'_{i}} \left(\left(\frac{\partial \Theta_{y,LB,i}}{\partial x'} \right)^{2} + \left(\frac{\partial \Theta_{x,LB,i}}{\partial y'} \right)^{2} \right) dA'_{i} - 2\nu_{i} \int_{A'_{i}} \frac{\partial \Theta_{y,LB,i}}{\partial x'} \frac{\partial \Theta_{x,LB,i}}{\partial y'} dA'_{i} + \cdots \right) dA'_{i} + \frac{1-\nu_{i}}{2} \int_{A'_{i}} \left(\frac{\partial \Theta_{y,LB,i}}{\partial y'} - \frac{\partial \Theta_{x,LB,i}}{\partial x'} \right)^{2} dA'_{i} \right) dA'_{i} dA'_{i} + \cdots$$

$$(58)$$

$$K_{s,LB,i} = \frac{k_s E_i \gamma_i a}{2(1 + \nu_i)} \int_{A_i'} \left(\left(\frac{\partial W_{LB,i}}{\partial x'} + \Theta_{y,LB,i} \right)^2 + \left(\frac{\partial W_{LB,i}}{\partial y'} - \Theta_{x,LB,i} \right)^2 \right) dA_i'$$
(59)

and

$$M_{\text{LB},i} = \rho_i \gamma_i a^3 \int_{A'_i} W_{\text{LB},i}^2 dA'_i + \frac{\rho_i \gamma_i^3 a^3}{12} \int_{A'_i} \left(\Theta_{x,\text{LB},i}^2 + \Theta_{y,\text{LB},i}^2\right) dA'_i$$
 (60)

where each equation is notably expressed as a set of integrals involving only $W_{LB,i}$, $\Theta_{x,LB,i}$, and $\Theta_{y,LB,i}$ and their x'- and y'-derivatives multiplied by constants for the mode section, since it is assumed that each section of the partition has a constant non-dimensional thickness γ_i and uniform material properties E_i , v_i , and ρ_i . It should also be noted that Eqs. (58) through (60) are valid for both the identified sections of the filler material determined in Section 4.2 and the matrix and resonator elements: in the latter scenario, all integrals except for that involving $W_{LB,i}$ in Eq. (60) vanish in the calculation,

since the rotation Bloch modes are very nearly equal to zero (e.g., Fig. 4) and the x'- and y'-derivatives of W_{LB} are likewise equal to zero (since the matrix and resonator are rigid elements) in the Bloch modes of the matrix and resonator materials. Defining the function $\mathcal{I}(\bullet) \equiv \int_{A'} (\bullet) dA'_i$ to be the surface integral of the argument of \mathcal{I} over the A'_i region (e.g., $\mathcal{I}(W_i^2) \equiv \int_{A'} (\bullet) dA'_i$ to be the surface integral of the argument of \mathcal{I} over the A'_i region (e.g., $\mathcal{I}(W_i^2) \equiv \int_{A'} (\bullet) dA'_i$) and the $\mathcal{I}(A)$ region (e.g., $\mathcal{I}(A)$) and the $\mathcal{I}(A)$ region (e.g., $\mathcal{I}(A)$) and the $\mathcal{I}(A)$ region (e.g., $\mathcal{I}(A)$) are likewise equal to zero (since the matrix and resonator are rigid elements) in the Bloch modes of the matrix and resonator materials.

 $\int_{A'_i} W_i^2 dA'_i$, Eqs. (58) through (60) can be rewritten as

$$K_{b,LB,i} = \frac{E_{i}\gamma_{i}^{3}a}{12(1-\nu_{i}^{2})} \left(\mathcal{I}\left(\frac{\partial\Theta_{y,LB,i}}{\partial x'}^{2}\right) - 2\nu_{i}\mathcal{I}\left(\frac{\partial\Theta_{y,LB,i}}{\partial x'}\frac{\partial\Theta_{x,LB,i}}{\partial y'}\right) + \mathcal{I}\left(\frac{\partial\Theta_{x,LB,i}}{\partial y'}^{2}\right) + \cdots + \frac{1-\nu_{i}}{2} \left(\mathcal{I}\left(\frac{\partial\Theta_{x,LB,i}}{\partial x'}^{2}\right) - 2\mathcal{I}\left(\frac{\partial\Theta_{x,LB,i}}{\partial x'}\frac{\partial\Theta_{y,LB,i}}{\partial y'}\right) + \mathcal{I}\left(\frac{\partial\Theta_{y,LB,i}}{\partial y'}^{2}\right) \right) \right)$$

$$(61)$$

$$K_{s,LB,i} = \frac{k_s E_i \gamma_i a}{2(1 + \nu_i)} \left(\mathcal{I} \left(\frac{\partial W_{LB,i}}{\partial x'}^2 \right) + 2\mathcal{I} \left(\Theta_{y,LB,i} \frac{\partial W_{LB,i}}{\partial x'} \right) + \mathcal{I} \left(\Theta_{y,LB,i}^2 \right) + \cdots \right.$$

$$\cdots + \mathcal{I} \left(\frac{\partial W_{LB,i}}{\partial y'}^2 \right) - 2\mathcal{I} \left(\Theta_{x,LB,i} \frac{\partial W_{LB,i}}{\partial y'} \right) + \mathcal{I} \left(\Theta_{x,LB,i}^2 \right)$$
(62)

and

$$M_{\text{LB},i} = \rho_i \gamma_i a^3 \mathcal{I}\left(W_{\text{LB},i}^2\right) + \frac{\rho_i \gamma_i^3 a^3}{12} \left(\mathcal{I}\left(\Theta_{x,\text{LB},i}^2\right) + \mathcal{I}\left(\Theta_{y,\text{LB},i}^2\right)\right)$$
(63)

in terms of the characteristic length a, non-dimensional element thicknesses γ_i , and material properties E_i , v_i , and ρ_i , along with the set of pre-computed integrals \mathcal{I} that do not change when any of the preceding metamaterial parameters are altered. These integrals \mathcal{I} can be easily computed by symbolic integration using the identified surface equations if a simple transformation exists between the (x', y') regions and the isoparametric sections (e.g., when all sections of the unit cell partition are rectangular regions), or by numerical integration if a transformation fostering simple symbolic integration cannot be found.

To obtain the values of K_b , K_s , and M at the upper bound of the BG, we exploit the fact that the displacement and rotation Bloch modes at the BG upper bound can be approximated almost exactly by those at the lower bound (an example illustrating this accuracy is provided in the following section), with the upper bound rotation mode shapes approximately equal to those at the lower bound and the upper bound displacement mode shape approximately equal to the lower bound displacement mode minus its center of mass. (Using our now continuous equations for the identified lower bound displacement Bloch mode, its center of mass can be computed quite easily in terms of the pre-computed integrals $\mathcal{I}\left(W_{LB,i}\right)$ and $\mathcal{I}\left(1\right)$ and the density and element thickness data for the unit cell, where $\mathcal{I}\left(1\right) \equiv \int_{A_i'} dA_i'$ is simply the area in the xy-plane of the ith section of the partition; this is shown in more detail in the Appendix in Eq. (A.5)). Using this, the following model can be assumed for approximating the upper bound Bloch modes W_{UB} , $\Theta_{x,UB}$, and $\Theta_{y,UB}$ using those at the lower bound to simplify the identification procedure:

$$W_{UB} \approx W_{LB} - z_{COM}, \ \Theta_{x,UB} \approx \Theta_{x,LB}, \ \text{and} \ \Theta_{y,UB} \approx \Theta_{y,LB}$$
 (64)

where z_{COM} denotes the center of mass of the lower bound displacement Bloch mode. Using Eq. (64), we notice that $\frac{\partial}{\partial x'}(\bullet)_{LB} \approx \frac{\partial}{\partial x'}(\bullet)_{UB}$ and $\frac{\partial}{\partial y'}(\bullet)_{LB} \approx \frac{\partial}{\partial y'}(\bullet)_{UB}$ for each non-dimensional Bloch mode (where (\bullet) here denotes W, Θ_x , or Θ_y), since z_{COM} is independent of x' and y'. Thus, under the assumption of Eq. (64), all of the integrals \mathcal{I} in Eqs. (61) and (62) are approximately equivalent at both bounds of the first BG, and therefore:

$$K_{b,UB,i} \approx K_{b,LB,i}$$
 and $K_{s,UB,i} \approx K_{s,LB,i}$ (65)

for all sections of the partition. Similarly, since the form of Eq. (63) is valid at either BG bound, all lower bound subscripts can be replaced with upper bound subscripts in this equation and Eq. (64) can be substituted to give

$$M_{\text{UB},i} \approx \rho_{i} \gamma_{i} a^{3} \left(\mathcal{I}\left(W_{\text{LB},i}^{2}\right) - 2 z_{\text{COM}} \mathcal{I}\left(W_{\text{LB},i}\right) + z_{\text{COM}}^{2} \mathcal{I}\left(1\right) \right) + \frac{\rho_{i} \gamma_{i}^{3} a^{3}}{12} \left(\mathcal{I}\left(\Theta_{x,\text{LB},i}^{2}\right) + \mathcal{I}\left(\Theta_{y,\text{LB},i}^{2}\right) \right)$$

$$(66)$$

describing the mass value at the upper bound of the BG for the ith section of the unit cell partition.

Using these values for K_b , K_s , and M at each section of the unit cell and at the lower and upper bounds of the first BG (Eqs. (61) through (66)), these computed expressions can be summed over the N sections of the partition to obtain the total bending stiffness, shear stiffness, and mass values at the Bloch modes of vibration corresponding to the lower and upper bounds of the first BG:

$$K_{b,\text{UB}} \approx K_{b,\text{LB}} = \sum_{i=1}^{N} K_{b,\text{LB},i}, \quad K_{s,\text{UB}} \approx K_{s,\text{LB}} = \sum_{i=1}^{N} K_{s,\text{LB},i}, \quad M_{\text{LB}} = \sum_{i=1}^{N} M_{\text{LB},i}, \quad \text{and} \quad M_{\text{UB}} = \sum_{i=1}^{N} M_{\text{UB},i}$$
 (67)

where $K_{b,LB,i}$, $K_{s,LB,i}$, $M_{LB,i}$, and $M_{UB,i}$ were defined in Eqs. (61), (62), (63), and (66), respectively. Finally, the values of K_b , K_s , and M at both bounds of the BG in Eq. (67) can be substituted into Eq. (28) to *instantaneously* compute the first BG of any metamaterial sharing the same reference geometry to the one originally employed in determining the non-dimensional Bloch modes—a procedure that will be exemplified in the following sections.

Table 1Unit cell parameters of the H–S–H metamaterial used in FEEA.

	Material	Elastic modulus E (Pa)	Poisson's ratio v	Mass density ρ (kg/m ³)	Non-dimensional thickness γ
Matrix	Aluminum	6.89×10^{10}	0.33	2700	0.10
Filler	Silicone rubber	1.00×10^{6}	0.49	1300	0.10
Resonator	Brass	1.06×10^{11}	0.32	8500	0.15

Table 2 Accuracy of identified solution.

	W_{LB}	$\Theta_{x,LB}$	$\Theta_{y,LB}$	W_{UB}	$\Theta_{x,UB}$	$\Theta_{y,UB}$
Maximum absolute error	0.34%	1.23%	1.23%	4.46%	2.66%	2.66%
RMS error	0.015%	0.051%	0.051%	1.35%	0.506%	0.506%
Average absolute error	0.009%	0.030%	0.030%	1.20%	0.427%	0.427%

5. Numerical results

Using the framework detailed in Sections 3 and 4, a numerical example of the system identification and BG computation algorithms is now presented, both to illustrate the accuracy of the identification analysis for a sample metamaterial and to demonstrate the utility of this method in algebraically computing the first BG of an infinite number of metamaterials with a *single* FEEA. To this end, the unit cell in Fig. 1 is employed to determine the non-dimensional Bloch modes for this specific reference geometry, defined by unit cell side lengths of a = b = 20 mm, an original filler side length of 16 mm, and an original resonator side length of 8 mm, with both the filler and resonator elements having square geometries. The material properties and non-dimensional element thicknesses used to determine these Bloch modes are shown in Table 1, where aluminum, soft silicone rubber, and brass are used as the matrix, filler, and resonator materials, respectively. A soft silicone rubber with an elastic modulus of 1 MPa is chosen as the filler material to provide a large difference in elastic moduli between the matrix and filler and the resonator and filler elements, ensuring a nearly perfect rigidity to the Bloch modes of the matrix and resonator materials at each BG bound; however, it will be shown later in this section that the Bloch modes of such a unit cell still provide excellent estimation of the first BG for unit cells of stiffer filler materials.

5.1. Identification solution

Using this H–S–H metamaterial with square filler and resonator elements, a single application of FEEA is employed to compute both the first BG and the displacement and rotation Bloch modes at the lower and upper BG bounds on a rectangular grid of data points, allowing the identification procedure described in Sections 4.2.1 through 4.2.4 to be used to fit surface equations to each of the partitioned sections (shown in Fig. 5). To conduct the identification procedure, a set of 7th-order polynomial basis functions in r and in s were chosen to form the respective basis function vectors $\mathbf{f}(r)$ and $\mathbf{g}(s)$ for each mode section, with periodic and higher order polynomial basis functions investigated but found to offer no significant improvements to identification accuracy over 7th-order polynomials. The results of this identification analysis are shown in Fig. 6, with Figs. 6a through c displaying the identified solutions for c0, and c1, and c2, and c3, and c4, and c5, and c6, and Figs. 6d through c6 displaying the identified solutions at the upper bound.

To evaluate the numerical accuracy of the identification, RMS, average absolute, and maximum absolute errors between the identified and FEEA solutions calculated using Eq. (57) are displayed in Table 2, with the RMS and absolute error equations expanded to account for the entire Bloch mode and with each error statistic displayed as a percentage of the maximum amplitude of the corresponding FEEA mode. The error plots represented by these summary statistics are presented below each corresponding identified Bloch mode in Fig. 6, with maximum absolute errors of only 0.34% for the lower bound displacement solution, 1.23% for the lower bound rotation solutions, 2.66% for the upper bound rotation solutions, and 4.46% for the upper bound displacement Bloch mode. The higher errors for the upper bound Bloch modes are not a reflection of the accuracy of the least squares analysis, but a simple result of the observation stated earlier that the upper bound modes can be approximated by those at the lower bound. In the lower bound Bloch modes (directly identified in the least squares procedure), the overall RMS errors providing a measure of the standard deviation of all identification errors are 0.015% and 0.051% for the displacement and rotation solutions, respectively, providing a nearlyexact identification of the lower bound Bloch modes using the least squares analysis. While not as accurate as the lower bound Bloch modes, the upper bound displacement and rotation solutions with overall RMS errors of 1.35% and 0.51%, respectively still provide a reasonable approximation of the upper bound Bloch modes, and it will be shown next that both these lower and upper bound solutions provide reliable estimation of the first BG for an infinite number of metamaterials despite the less accurate identification solution at the upper bound.

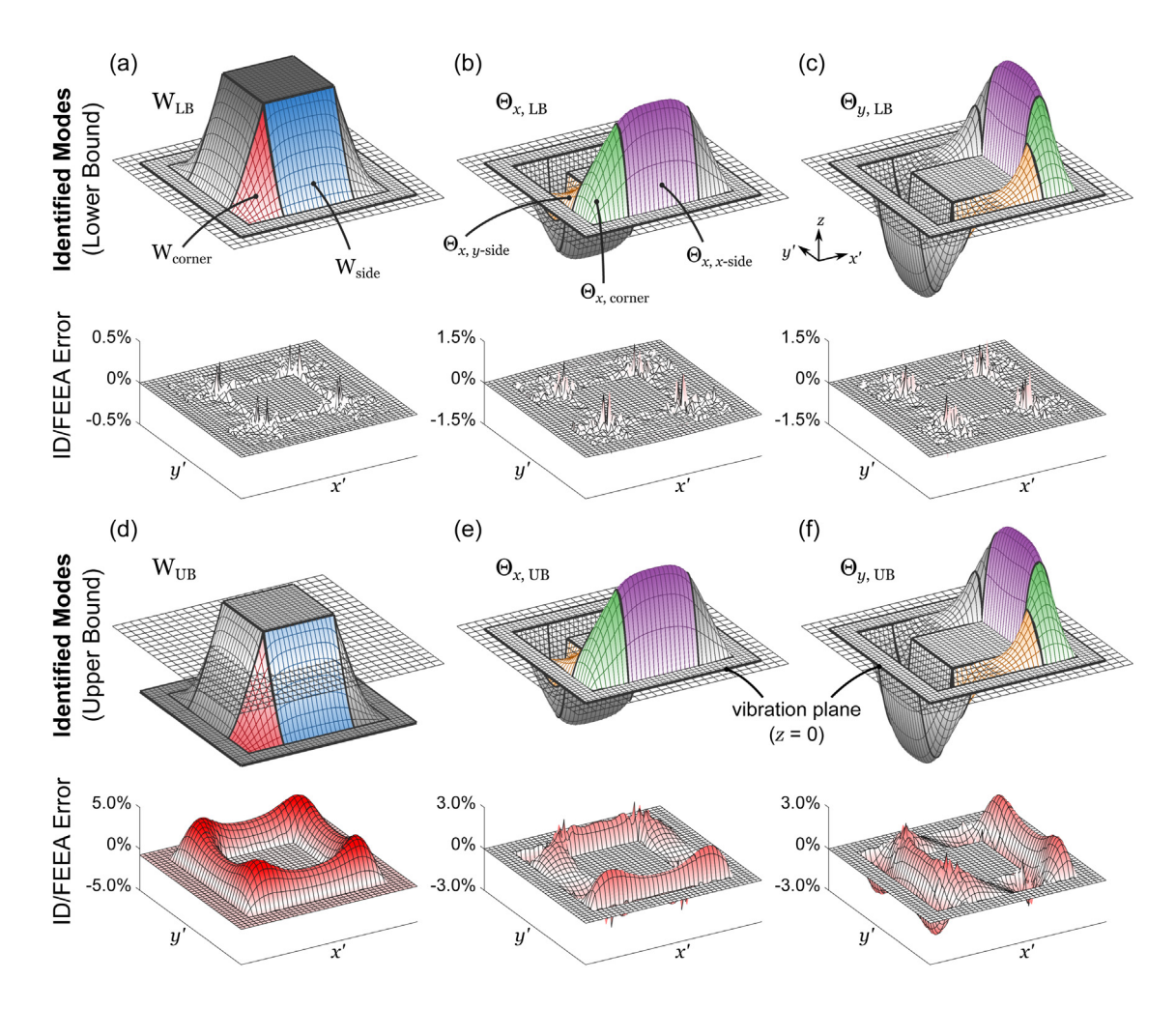


Fig. 6. Identification results and errors between FEEA and identified solutions displayed for the non-dimensional displacement and rotation Bloch mode shapes of a sample H-S-H metamaterial at the lower and upper bounds of the first BG. Vertical axes on error plots display the error between identified and FEEA solutions as a percentage of the maximum value of the FEEA-computed mode shape. Color scales are identical for each error plot and range from white at zero error to red at $\pm 4.5\%$ error between the FEEA and identified mode shape solutions. Colored sections of the mode shapes represent the sections of the lower bound W and Θ_x modes identified directly from the FEEA solutions, matching the sections shown in Fig. 5.

5.2. BG computation using identified Bloch modes

Using the identified non-dimensional Bloch modes for the original H–S–H metamaterial, we now make use of the BG computation method presented in Sections 3.3 and 4.3 to demonstrate computation of the first BG in an *infinite number* of metamaterials using only the identified Bloch modes and algebraic expressions involving the material and geometric properties of each unit cell. To achieve this, we present nine examples in which this method can be applied to compute the first BG in many metamaterials with a single application of FEEA and the identification analysis. In Example 1, the first BG of the original metamaterial is estimated using Eqs. (61) through (67) of Section 4.3 and Eq. (28) of Section 3.3 to compute the stiffness and mass values and the corresponding BG frequencies for the metamaterial, yielding a BG of 216.4 to 367.3 Hz in the identified solution. (More specific details on how to determine this BG are presented in Section 6). Meanwhile, the BG computed by FEEA in the original computation yielded a BG of 211.3 to 358.1 Hz, corresponding to lower and upper bound BG frequency errors of 2.38% and 2.59%, respectively. The small significance of these errors relative to the size of the BG and band structure can be evidenced from Fig. 7a, showing the first four bands of the band structure computed by FEEA (using a 20×20 mesh of quadrilateral, 8-node serendipity elements), the FEEA-computed BG indicated by the shaded region, and the identified BG indicated by the solid blue circles at the M and Γ points of the IBZ.

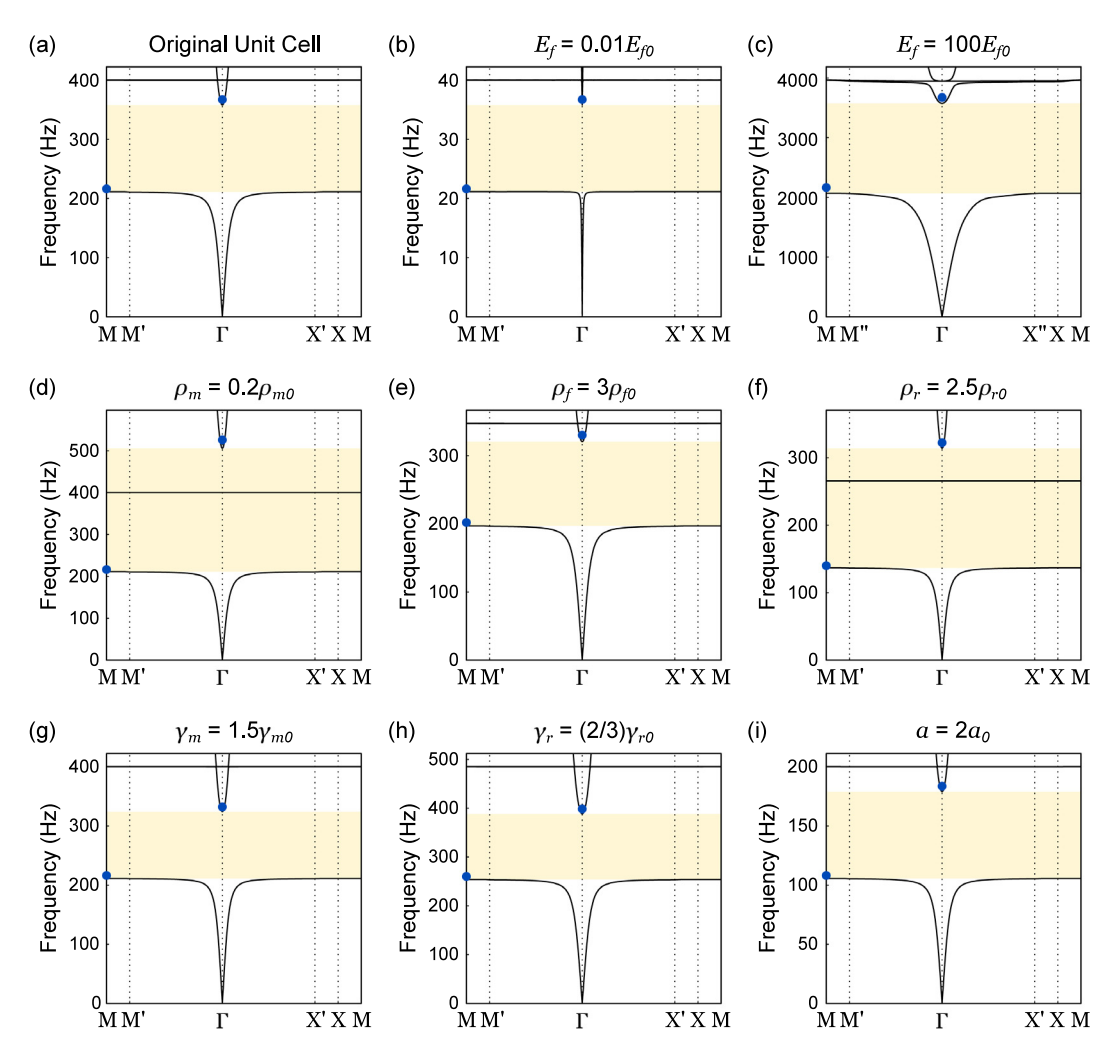


Fig. 7. Comparison of band structures and BGs for sample H–S–H metamaterials computed with FEEA and the presented identification algorithm. Bands and highlighted BGs (shaded regions) were computed by FEEA using a 20 × 20 finite element mesh of quadrilateral, 8-node serendipity elements; solid blue circles represent the BG bounds computed with the system identification method using the Bloch modes at the lower bound of the original unit cell. M' and X' are defined as the points on the IBZ boundary with non-dimensional wavenumbers $\tilde{k}_x = \tilde{k}_y = \pi/(5\sqrt{2})$ and $\tilde{k}_x = \pi/5$, $\tilde{k}_y = 0$, respectively (Fig. 1c), while M'' and X'' in Fig. 7c are defined by $\tilde{k}_x = \tilde{k}_y = 4\pi/(5\sqrt{2})$ and $\tilde{k}_x = 4\pi/5$, $\tilde{k}_y = 0$, respectively.

To demonstrate the applicability of this approach in computing BGs for other metamaterials without additional application of FEEA, the band structure and identified first BG for Examples 2 through 9 are shown in Figs. 7b through i, respectively, with the numerical results for each FEEA and identified BG and the errors between them presented in Fig. 8 for all scenarios. (The FEEA band structures and BGs are presented simply as verification of the identification solution; they are not required to be computed nor identified in the computation procedure). Example 2 in Fig. 7b presents the case where the elastic modulus of the filler material E_f has been modified to 1% of its original value, showing a BG shift to exactly 1/10 of the BG frequencies in the original metamaterial and lower and upper BG bound errors between the FEEA and identification solutions of 2.34% and 2.59%, respectively. Similarly, Example 3 in Fig. 7c analyzes a filler elastic modulus modified to 100 times its original value ($E_f = 100E_{f0}$), showing a BG shift to exactly 10 times the original BG frequencies and lower and upper BG bound errors of 4.67% and 2.82%, respectively. Here, we notice that despite the increased stiffness of the filler material, this BG computation method still provides a reliable (albeit with greater lower bound error) estimate of the first BG, even though the elastic modulus of the filler material is in this scenario slightly closer to that of the matrix and resonator materials ($E_m = 68.9$ GPa, $E_r = 106$ GPa, and $E_f = 100$ MPa)—that is, the filler elastic modulus E_f is still low enough to yield an accurate estimation of the first BG by this procedure. Further, we note that it is no coincidence that a decrease in E_f by a factor of 100 decreases the BG frequencies by a factor 10, while an increase in E_f by a factor of 100 increases the BG frequencies by a factor 10. In fact, it can be shown by a simple manipulation of the algebraic equations for K_b , K_s , and M in Eqs. (61) through (67) and (28) that any modification to the elastic modulus of the filler material by a factor of n yields a variation in both the lower and upper bound BG frequencies

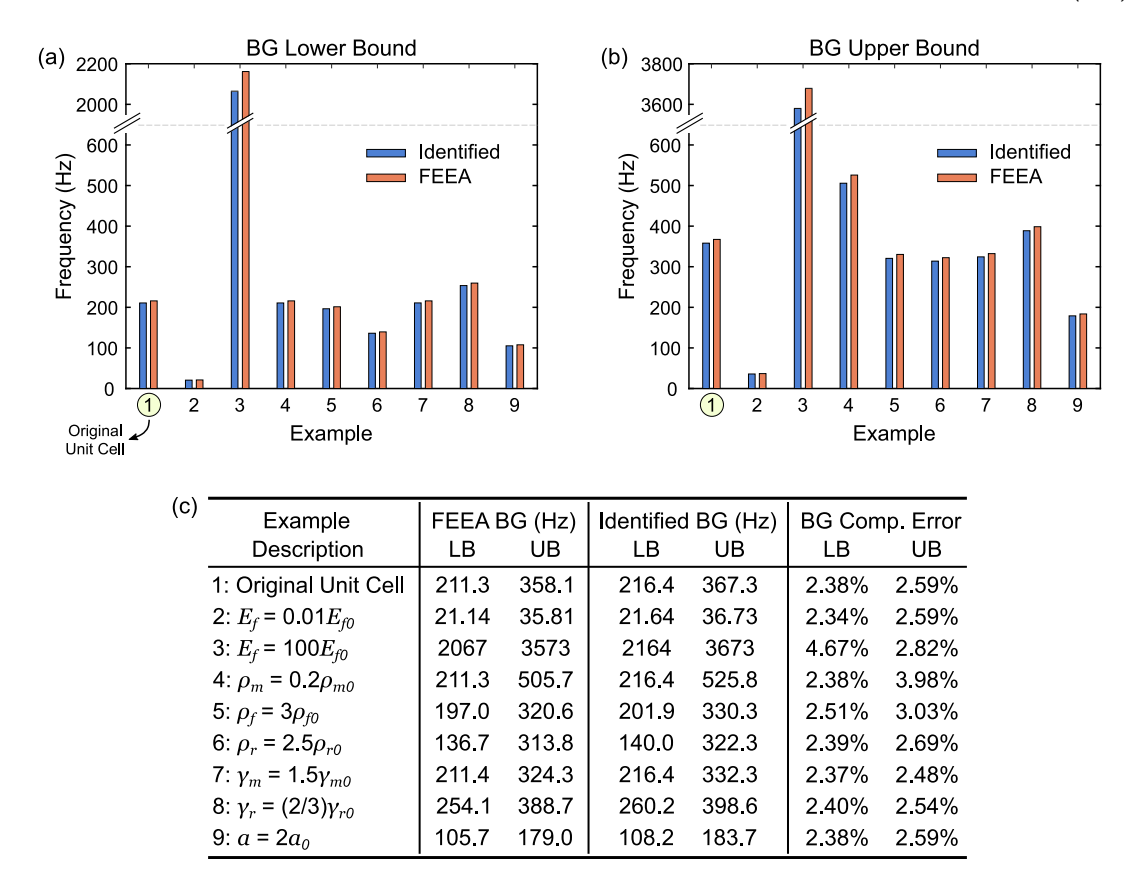


Fig. 8. Identified and FEEA BG frequencies corresponding to the (a) lower and (b) upper BG bounds in the original unit cell (Example 1) and the remaining H–S–H metamaterial designs analyzed in Sections 5 and 7. (c) Numerical solutions for both BG bounds and the computational errors associated with each design.

by a factor of \sqrt{n} for H–S–H metamaterials of sufficiently soft filler material, yielding a relation between the filler elastic modulus and the first BG of H–S–H metamaterials that would be very useful in applications investigating the effects of metamaterial parameters on BG frequencies—for example, when analyzing soft, variable-stiffness filler elements utilized in tunable H–S–H metamaterials [27–30]. (These relationships can be evidenced most clearly from the equations that will be presented in Section 6).

In the remaining presented scenarios, Examples 4 through 6 demonstrate that modification to the mass densities of any constitutive material can be made without compromising the accuracy of the computation, with Example 4 demonstrating a decrease in the matrix material density by a factor of 5 (Fig. 7d) and Examples 5 and 6 demonstrating an increase in the filler and resonator material densities by factors of 3 and 2.5, respectively (Figs. 7e and f). When varying the matrix and resonator material densities in Examples 4 and 6, modification to the Bloch modes corresponding to the flat band shown above the upper BG bound in other cases causes this band to lie within instead of above the first BG, separating the now wider BG into two distinct regions (as was discussed in Section 2). However, the identification procedure still accurately predicts the lower and upper bounds of the larger BG formed on the two sides of this flat band (Figs. 7d and f). Further, Example 7 in Fig. 7g and Example 8 in Fig. 7h demonstrate modification to the non-dimensional thicknesses of the matrix and resonator elements, respectively (recall from Section 2 that changes to the non-dimensional filler thickness are not allowed in this BG computation procedure), and Example 9 in Fig. 7i demonstrates an increase in unit cell size achieved by doubling the unit cell's characteristic length, which is found to decrease the BG frequencies by a factor of 2 in the identified solution. Expanding this result, one can easily show using the equations of Sections 3.3 and 4.3 that a modification to the unit cell characteristic length by a factor of n yields a variation in the lower and upper BG frequencies by a factor of 1/n, demonstrating another useful relation evident from the BG equations which can be used as a simple design rule when designing H-S-H metamaterials to have specific BGs (see Section 6). Finally, we note that any two or more of these modifications to the original metamaterial can be made and provide an accurate estimation of the first BG for the new design, along with any modifications to the matrix and resonator elastic moduli and the Poisson's ratio of any material. This provides a useful procedure for computing the first BG of any similar metamaterial from a single FEEA as well as algebraic relationships between the metamaterial's material properties, element thicknesses, and unit cell size, which can be used to both simultaneously compute BGs in a large number of metamaterials and produce design strategies for creating H-S-H metamaterials with specific BG properties.

6. Application: Designing an H-S-H metamaterial with a specified band gap

To further exemplify the application of our BG prediction method, we now present one final example employing the procedure in designing metamaterials with specific BG properties. Suppose we are in search of a metamaterial with a BG from 100 to 200 Hz and we have selected an H–S–H configuration with aluminum, silicone rubber, and brass with material properties in Table 1 as the materials for the matrix, filler, and resonator elements, respectively. Suppose also that we design the metamaterial with square filler and resonator elements and the same reference geometry used to compute the non-dimensional Bloch modes shown earlier in this paper. Doing so reduces the unspecified parameters of the unit cell to the non-dimensional matrix thickness γ_m , the non-dimensional resonator thickness γ_r , and the unit cell characteristic length α , all of which can be analyzed using the results of Sections 3 and 4 to obtain a specific combination that produces a metamaterial with the desired BG.

After algebraic manipulation of Eqs. (61) through (67) and (28) (shown in the Appendix), expressions for the lower and upper bounds of the first BG can be shown to be:

$$f_{LB} = \frac{\sqrt{E_f}}{2\pi a} \left(\frac{\left[1 - \nu_f^2\right]^{-1} \gamma_f^3 \left(I_{1,c} + I_{1,s}\right) + 6\left[1 + \nu_f\right]^{-1} k_s \gamma_f \left(I_{2,c} + I_{2,s}\right)}{12 \rho_f \gamma_f \left(I_{3,c} + I_{3,s}\right) + 3 \rho_r \gamma_r I_{3,r} + \rho_f \gamma_f^3 \left(I_{6,c} + I_{6,s}\right)} \right)^{1/2}$$
(68a)

$$f_{\text{UB}} = \frac{\sqrt{E_f}}{2\pi a} \left(\frac{\left[1 - \nu_f^2\right]^{-1} \gamma_f^3 \left(I_{1,c} + I_{1,s}\right) + 6\left[1 + \nu_f\right]^{-1} k_s \gamma_f \left(I_{2,c} + I_{2,s}\right)}{12 \rho_f \gamma_f \left(I_{3,c} + I_{3,s}\right) + 3 \rho_r \gamma_r I_{3,r} + \rho_f \gamma_f^3 \left(I_{6,c} + I_{6,s}\right) + 3 f(\rho, \gamma, I_4, I_5)} \right)^{1/2}$$
(68b)

where $f(\rho, \gamma, I_4, I_5)$ is defined as

$$f(\rho, \gamma, I_4, I_5) \equiv -\frac{\left(4\rho_f \gamma_f \left(I_{4,c} + I_{4,s}\right) + \rho_r \gamma_r I_{4,r}\right)^2}{4\rho_f \gamma_f \left(I_{5,c} + I_{5,s}\right) + \rho_r \gamma_r I_{5,r} + \rho_m \gamma_m I_{5,m}}$$
(69)

and I_1 through I_6 are defined as

$$I_{1}\left(\nu_{i},\Theta_{x,LB,i},\Theta_{y,LB,i}\right) \equiv \mathcal{I}\left(\frac{\partial\Theta_{y,LB,i}}{\partial x'}^{2}\right) - 2\nu_{i}\mathcal{I}\left(\frac{\partial\Theta_{y,LB,i}}{\partial x'}\frac{\partial\Theta_{x,LB,i}}{\partial y'}\right) + \mathcal{I}\left(\frac{\partial\Theta_{x,LB,i}}{\partial y'}^{2}\right) + \cdots$$

$$\cdots + \frac{1-\nu_{i}}{2}\left(\mathcal{I}\left(\frac{\partial\Theta_{x,LB,i}}{\partial x'}^{2}\right) - 2\mathcal{I}\left(\frac{\partial\Theta_{x,LB,i}}{\partial x'}\frac{\partial\Theta_{y,LB,i}}{\partial y'}\right) + \mathcal{I}\left(\frac{\partial\Theta_{y,LB,i}}{\partial y'}^{2}\right)\right)$$

$$(70a)$$

$$I_{2}\left(W_{LB,i},\Theta_{x,LB,i},\Theta_{y,LB,i}\right) \equiv \mathcal{I}\left(\frac{\partial W_{LB,i}}{\partial x'}^{2}\right) + 2\mathcal{I}\left(\Theta_{y,LB,i}\frac{\partial W_{LB,i}}{\partial x'}\right) + \mathcal{I}\left(\Theta_{y,LB,i}^{2}\right) + \dots$$

$$\dots + \mathcal{I}\left(\frac{\partial W_{LB,i}}{\partial y'}^{2}\right) - 2\mathcal{I}\left(\Theta_{x,LB,i}\frac{\partial W_{LB,i}}{\partial y'}\right) + \mathcal{I}\left(\Theta_{x,LB,i}^{2}\right)$$

$$(70b)$$

$$I_{3}\left(\mathsf{W}_{\mathsf{LB},i}\right) \equiv \mathcal{I}\left(\mathsf{W}_{\mathsf{LB},i}^{2}\right) \tag{70c}$$

$$I_4\left(\mathsf{W}_{\mathsf{LB},i}\right) \equiv \mathcal{I}\left(\mathsf{W}_{\mathsf{LB},i}\right) \tag{70d}$$

$$I_{5} \equiv \mathcal{I}(1) \tag{70e}$$

$$I_{6}\left(\Theta_{x,LB,i},\Theta_{y,LB,i}\right) \equiv \mathcal{I}\left(\Theta_{x,LB,i}^{2}\right) + \mathcal{I}\left(\Theta_{y,LB,i}^{2}\right) \tag{70f}$$

with the integrals $\mathcal{I}(\bullet)$ pre-computed using symbolic or numerical integration from the identified Bloch modes for the reference geometry (and $\mathcal{I}(\bullet)$ was defined in Section 4.3). Note in these equations that for any $n \in \{1, 2, ..., 6\}$, $I_{n,c}$ refers to I_n evaluated on the corner section of the filler material, $I_{n,s}$ refers to I_n evaluated on the side section of the filler material, $I_{n,m}$ refers to I_n evaluated on the resonator material of the reference unit cell. Since all integral functions I_n are constant for the reference geometry, Eqs. (68) through (70) can now be used to provide algebraic relationships between unit cell parameters and BG bounds to serve numerous applications in both analysis and design of H–S–H metamaterials. (Eqs. (68) through (70) are precisely the equations used to compute the identified BGs for sample metamaterials and identify relationships between unit cell parameters and BG frequencies analyzed in Section 5).

To illustrate the application of these equations in designing metamaterials, consider our example of designing an H–S–H metamaterial with a BG from 100 to 200 Hz in which all unit cell parameters with the exceptions of γ_m , γ_r , and a have been selected, and we aim to choose specific values for γ_m , γ_r , and a that yield an H–S–H metamaterial with the desired BG. Suppose we further specify that our metamaterial has a non-dimensional resonator thickness of 0.3, which—since Eq. (68a) for f_{LB} depends on a and γ_r but not γ_m —allows us to directly solve Eq. (68a) for a and determine the unit cell characteristic length with $\gamma_r = 0.3$ that predicts a BG lower bound of 100 Hz. With both a and γ_r determined, we can then substitute those values into Eq. (68b) for f_{LB} to determine the non-dimensional matrix thickness that gives a BG upper bound of 200 Hz. Following this approach using pre-computed integrals of the identified Bloch modes yields

 $a=31.182~{
m mm}$ and $\gamma_m=0.12138$, which combined with the specified value $\gamma_r=0.3$, the chosen material properties, and the reference geometry yields all parameters for an H–S–H metamaterial with a predicted BG from 100 to 200 Hz using our novel method. Verifying the BG of this metamaterial using the finite element mesh in Section 5 yields an FEEA-computed BG from 97.68 to 194.9 Hz with a flat intermediate band at 163.1 Hz—a result that yields less than 2.6% error between solutions at both BG bounds and validates the accuracy of this method in both efficiently computing BGs and designing metamaterials with specific BG properties.

7. Summary and conclusions

This paper has examined BG formation mechanisms in two-dimensional locally resonant elastic metamaterials and presented an approach for computing the first frequency BG in metamaterials with:

- 1. Out-of-plane material motion (transverse vibrations)
- 2. H-S-H design with square matrix, filler, and resonator elements (implying unit cell symmetry)
- 3. Through-thickness unit cell geometry (any (x, y) location has uniform properties in the z-direction so 2D analysis can be utilized)

H-S-H configurations subject to transverse vibrations were selected for this analysis due to their versatility in twodimensional metamaterial design and their similarities in Bloch modes at the lower and upper bounds of the first BG. It was observed that all H-S-H metamaterials of specific planar geometry and ratio of filler thickness to unit cell size yield the same non-dimensional out-of-plane Bloch mode shapes in all metamaterials of any matrix or resonator thicknesses, unit cell size, or material properties. These observations were shown to be a consequence of the fact that all H-S-H unit cells of soft filler material consist of a rigid matrix and resonator vibrating around a deforming filler material at pass band solutions at the lower and upper bounds of the first BG. Inspired by these similarities, a method was presented to compute vibration frequencies corresponding to these Bloch modes using Mindlin plate theory and conservation of energy principles. A least squares identification algorithm was detailed for computing continuous surface equations for the mode shapes, which were employed in the preceding equations to compute the first BG frequencies. The framework was applied to nine different metamaterials with rectangular unit cells, and the computation of the first BG was achieved using a single finite element eigenfrequency analysis (FEEA) with high numerical accuracy. The same computations used to calculate the first BG also reveal sensitivities between metamaterial parameters and BG frequencies in the form of simple algebraic relationships, providing the ability to create computationally-instantaneous parametric studies and design choices for metamaterials with prespecified BGs. The procedure outlined here opens up new avenues in the predictive, rapid, and on-demand design of H-S-H unit cells with more general planar geometries, metamaterials with higher-order transverse or in-plane frequency BGs, and other configurations of locally resonant metamaterials.

CRediT authorship contribution statement

A. Ragonese: Conceptualization, Methodology, Writing - original draft. **M. Nouh:** Visualization, Resources, Project administration, Funding acquisition, Writing - review & editing.

Acknowledgments

The authors acknowledge support of this work from the US National Science Foundation through awards no. 1847254 (CAREER) and 1904254 as well as the NYS Center of Excellence in Materials Informatics (CMI).

Appendix

Deriving algebraic equations for BG bounds

In Sections 3, 4, and 6, it was shown that a set of algebraic relationships for the lower and upper bounds of the first BG could be computed from material properties, geometric properties, and pre-computed integrals of expressions involving non-dimensional Bloch modes, with Eqs. (68) through (70) in Section 6 providing a final concise form for these expressions. Here, an analytical derivation is presented that was used to arrive at these equations.

Using the integrals I_1 through I_6 defined in Eq. (70), the stiffness and mass values $K_{b,LB,i}$, $K_{s,LB,i}$, $M_{LB,i}$, and $M_{UB,i}$ derived in Eqs. (61) through (63) and (66) can be rewritten as

$$K_{b,LB,i} = \frac{E_i \gamma_i^3 a}{12(1 - \nu_i^2)} I_1 \left(\nu_i, \Theta_{x,LB,i}, \Theta_{y,LB,i} \right)$$
(A.1)

$$K_{s,LB,i} = \frac{k_s E_i \gamma_i a}{2(1+\nu_i)} I_2 \left(W_{LB,i}, \Theta_{x,LB,i}, \Theta_{y,LB,i} \right)$$
(A.2)

$$M_{\mathrm{LB},i} = \rho_i \gamma_i a^3 I_3 \left(W_{\mathrm{LB},i} \right) + \frac{\rho_i \gamma_i^3 a^3}{12} I_6 \left(\Theta_{\mathrm{x,LB},i}, \Theta_{\mathrm{y,LB},i} \right) \tag{A.3}$$

$$M_{\text{UB},i} = \rho_{i} \gamma_{i} a^{3} \left(I_{3} \left(W_{\text{LB},i} \right) - 2 z_{\text{COM}} I_{4} \left(W_{\text{LB},i} \right) + z_{\text{COM}}^{2} I_{5} \right) + \frac{\rho_{i} \gamma_{i}^{3} a^{3}}{12} I_{6} \left(\Theta_{x,\text{LB},i}, \Theta_{y,\text{LB},i} \right)$$

$$= M_{\text{LB},i} + \rho_{i} \gamma_{i} a^{3} \left(-2 z_{\text{COM}} I_{4} \left(W_{\text{LB},i} \right) + z_{\text{COM}}^{2} I_{5} \right)$$
(A.4)

Using the standard definition of center of mass, the integrals I_4 and I_5 in Eq. (70), the fact that the Bloch mode of the matrix material for W_{LB} is zero (i.e., $I_{4,m} \equiv \mathcal{I}(W_{LB,m}) = 0$), and the observation that the filler material consists of exactly four "corner" and four "side" sections, the center of mass z_{COM} of the lower bound displacement Bloch mode can be expressed as

$$z_{\text{COM}} = \frac{1}{\int_{A'} \rho \gamma \, a dA'} \int_{A'} \rho \gamma \, a W_{\text{LB}} dA' = \left[\sum_{i=1}^{N} \rho_{i} \gamma_{i} a \int_{A'} dA' \right]^{-1} \sum_{i=1}^{N} \rho_{i} \gamma_{i} a \int_{A'} W_{\text{LB},i} dA'$$

$$= \left[\sum_{i=1}^{N} \rho_{i} \gamma_{i} \mathcal{I} (1) \right]^{-1} \sum_{i=1}^{N} \rho_{i} \gamma_{i} \mathcal{I} (W_{\text{LB},i}) = \frac{4 \rho_{f} \gamma_{f} (I_{4,c} + I_{4,s}) + \rho_{r} \gamma_{r} I_{4,r}}{4 \rho_{f} \gamma_{f} (I_{5,c} + I_{5,s}) + \rho_{r} \gamma_{r} I_{5,r} + \rho_{m} \gamma_{m} I_{5,m}}$$
(A.5)

Summing $K_{b,LB,i}$ and $K_{s,LB,i}$ in Eqs. (A.1) and (A.2) over all sections of the unit cell and using the fact that I_1 and I_2 are zero for the matrix and resonator materials then yields the following for $K_{b,LB}$ and $K_{s,LB}$:

$$K_{b,LB} \equiv \sum_{i=1}^{N} K_{b,LB,i} = \frac{E_f \gamma_f^3 a}{12(1 - \nu_f^2)} \left(4I_{1,c} + 4I_{1,s} \right) = \frac{E_f \gamma_f^3 a}{3(1 - \nu_f^2)} \left(I_{1,c} + I_{1,s} \right)$$
(A.6)

$$K_{s,LB} \equiv \sum_{i=1}^{N} K_{s,LB,i} = \frac{k_s E_f \gamma_f a}{2(1 + \nu_f)} \left(4I_{2,c} + 4I_{2,s} \right) = \frac{2k_s E_f \gamma_f a}{1 + \nu_f} \left(I_{2,c} + I_{2,s} \right)$$
(A.7)

The fact that I_3 is zero for the matrix material and I_6 is zero for the matrix and resonator materials yields the following for M_{LB} :

$$M_{LB} \equiv \sum_{i=1}^{N} M_{LB,i} = \rho_f \gamma_f a^3 \left(4I_{3,c} + 4I_{3,s} \right) + \rho_r \gamma_r a^3 I_{3,r} + \frac{\rho_f \gamma_f^3 a^3}{12} \left(4I_{6,c} + 4I_{6,s} \right)$$

$$= 4\rho_f \gamma_f a^3 \left(I_{3,c} + I_{3,s} \right) + \rho_r \gamma_r a^3 I_{3,r} + \frac{\rho_f \gamma_f^3 a^3}{3} \left(I_{6,c} + I_{6,s} \right)$$
(A.8)

And the fact that I_4 and I_5 are zero for the matrix material yields the following for M_{UB} :

$$M_{\text{UB}} \equiv \sum_{i=1}^{N} M_{\text{UB},i} = M_{\text{LB}} + \sum_{i=1}^{N} \rho_{i} \gamma_{i} a^{3} \left(-2z_{\text{COM}} I_{4} \left(W_{\text{LB},i} \right) + z_{\text{COM}}^{2} I_{5} \right)$$

$$= M_{\text{LB}} + a^{3} \left(-2z_{\text{COM}} \sum_{i=1}^{N} \rho_{i} \gamma_{i} I_{4} \left(W_{\text{LB},i} \right) + z_{\text{COM}}^{2} \sum_{i=1}^{N} \rho_{i} \gamma_{i} I_{5} \right)$$

$$= M_{\text{LB}} + a^{3} \left(-2z_{\text{COM}} \left(4\rho_{f} \gamma_{f} \left(I_{4,c} + I_{4,s} \right) + \rho_{r} \gamma_{r} I_{4,r} \right) + z_{\text{COM}}^{2} \left(4\rho_{f} \gamma_{f} \left(I_{5,c} + I_{5,s} \right) + \rho_{r} \gamma_{r} I_{5,r} + \rho_{m} \gamma_{m} I_{5,m} \right) \right)$$

$$= M_{\text{LB}} + a^{3} \left(-2 \frac{4\rho_{f} \gamma_{f} \left(I_{4,c} + I_{4,s} \right) + \rho_{r} \gamma_{r} I_{4,r}}{4\rho_{f} \gamma_{f} \left(I_{5,c} + I_{5,s} \right) + \rho_{r} \gamma_{r} I_{5,r} + \rho_{m} \gamma_{m} I_{5,m}} \left(4\rho_{f} \gamma_{f} \left(I_{4,c} + I_{4,s} \right) + \rho_{r} \gamma_{r} I_{4,r} \right) + \cdots \right)$$

$$\cdots + \left(\frac{4\rho_{f} \gamma_{f} \left(I_{4,c} + I_{4,s} \right) + \rho_{r} \gamma_{r} I_{4,r}}{4\rho_{f} \gamma_{f} \left(I_{5,c} + I_{5,s} \right) + \rho_{r} \gamma_{r} I_{5,r} + \rho_{m} \gamma_{m} I_{5,m}} \right)^{2} \left(4\rho_{f} \gamma_{f} \left(I_{5,c} + I_{5,s} \right) + \rho_{r} \gamma_{r} I_{5,r} + \rho_{m} \gamma_{m} I_{5,m} \right) \right)$$

$$= M_{\text{LB}} - a^{3} \frac{\left(4\rho_{f} \gamma_{f} \left(I_{4,c} + I_{4,s} \right) + \rho_{r} \gamma_{r} I_{4,r} \right)^{2}}{4\rho_{f} \gamma_{f} \left(I_{5,c} + I_{5,s} \right) + \rho_{r} \gamma_{r} I_{4,r} \right)^{2}} = M_{\text{LB}} + a^{3} f(\rho, \gamma, I_{4}, I_{5})$$

using Eq. (A.5), where $f(\rho, \gamma, I_4, I_5)$ was defined in Eq. (69) of Section 6.

Letting $K_b = K_{b,LB}$, $K_s = K_{s,LB}$, and $M = M_{LB}$ for the lower bound of the BG and substituting Eqs. (A.6) through (A.8) into Eq. (28) then gives the equation

$$f_{LB} = \frac{1}{2\pi} \sqrt{\frac{K_{b,LB} + K_{s,LB}}{M_{LB}}} = \frac{1}{2\pi} \left(\frac{\frac{E_f \gamma_f^3 a}{3(1 - \nu_f^2)} \left(I_{1,c} + I_{1,s} \right) + \frac{2k_s E_f \gamma_f a}{1 + \nu_f} \left(I_{2,c} + I_{2,s} \right)}{4\rho_f \gamma_f a^3 \left(I_{3,c} + I_{3,s} \right) + \rho_r \gamma_r a^3 I_{3,r} + \frac{\rho_f \gamma_f^3 a^3}{3} \left(I_{6,c} + I_{6,s} \right)} \right)^{1/2}$$

$$= \frac{\sqrt{E_f}}{2\pi a} \left(\frac{\left[1 - \nu_f^2 \right]^{-1} \gamma_f^3 \left(I_{1,c} + I_{1,s} \right) + 6 \left[1 + \nu_f \right]^{-1} k_s \gamma_f \left(I_{2,c} + I_{2,s} \right)}{12\rho_f \gamma_f \left(I_{3,c} + I_{3,s} \right) + 3\rho_r \gamma_r I_{3,r} + \rho_f \gamma_f^3 \left(I_{6,c} + I_{6,s} \right)} \right)^{1/2}$$
(A.10)

producing the final expression for f_{LB} as stated in Eq. (68a) of Section 6.

Finally, letting $K_b = K_{b,UB}$, $K_s = K_{s,UB}$, and $M = M_{UB}$ for the upper bound of the BG, employing the assumptions that $K_{b,UB} \approx K_{b,LB}$ and $K_{s,UB} \approx K_{s,LB}$ as explained in Section 4.3 (Eq. (67)), and substituting Eqs. (A.6), (A.7), and (A.9) into Eq. (28) gives the equation

$$f_{\text{UB}} = \frac{1}{2\pi} \sqrt{\frac{K_{b,\text{UB}} + K_{s,\text{UB}}}{M_{\text{UB}}}} = \frac{1}{2\pi} \sqrt{\frac{K_{b,\text{LB}} + K_{s,\text{LB}}}{M_{\text{UB}}}}$$

$$= \frac{1}{2\pi} \left(\frac{\frac{E_{f} \gamma_{f}^{3} a}{3(1 - \nu_{f}^{2})} \left(I_{1,c} + I_{1,s} \right) + \frac{2k_{s} E_{f} \gamma_{f} a}{1 + \nu_{f}} \left(I_{2,c} + I_{2,s} \right)}{4\rho_{f} \gamma_{f} a^{3} \left(I_{3,c} + I_{3,s} \right) + \rho_{r} \gamma_{r} a^{3} I_{3,r} + \frac{\rho_{f} \gamma_{f}^{3} a^{3}}{3} \left(I_{6,c} + I_{6,s} \right) + a^{3} f(\rho, \gamma, I_{4}, I_{5})} \right)^{1/2}$$

$$= \frac{\sqrt{E_{f}}}{2\pi a} \left(\frac{\left[1 - \nu_{f}^{2} \right]^{-1} \gamma_{f}^{3} \left(I_{1,c} + I_{1,s} \right) + 6 \left[1 + \nu_{f} \right]^{-1} k_{s} \gamma_{f} \left(I_{2,c} + I_{2,s} \right)}{12\rho_{f} \gamma_{f} \left(I_{3,c} + I_{3,s} \right) + 3\rho_{r} \gamma_{r} I_{3,r} + \rho_{f} \gamma_{f}^{3} \left(I_{6,c} + I_{6,s} \right) + 3f(\rho, \gamma, I_{4}, I_{5})} \right)^{1/2}$$

producing the final expression for f_{UB} as stated in Eq. (68b) of Section 6.

Note on finite element analyses

Finite element analyses employed in this paper were completed using in-house MATLAB codes with 8-node serendipity or 12-node cubic two-dimensional quadrilateral Mindlin elements, with the specific element type selected depending on application. A 20×20 mesh of 12-node cubic elements was used to generate the band structure shown in Fig. 1 and the displacement and rotation Bloch modes shown in Figs. 2, 4, 5, and 6, which were used as the non-dimensional Bloch modes for all system identification and BG computation analyses performed in this paper. Due to its reduced computation time without significant loss of accuracy, a 20×20 mesh of 8-node serendipity elements was used to compute all FEEA BGs and band structures in Section 5 (Figs. 7 and 8) and Section 6, with the chosen mesh type yielding insignificant (less than 0.4%) differences in BG frequencies with the former mesh but more than 4 times reduction in computation time for a single eigenfrequency analysis. BG frequencies were found to be approximately 0.35% lower using a 20×20 cubic element mesh over a similar 10×10 mesh but only 0.09% lower using a 30×30 cubic element mesh over a similar 20×20 mesh, informing our selection of a 20×20 mesh showing sufficient convergence as our mesh size of choice in all finite element analyses. Pilot simulations using 3D elements were performed on H–S–H metamaterials in COMSOL Multiphysics and compared with our MATLAB analysis to confirm that the results of our in-house code are in agreement with commercially-proven software.

References

- [1] M.I. Hussein, M.J. Leamy, M. Ruzzene, Dynamics of phononic materials and structures: Historical origins, recent progress, and future outlook, Appl. Mech. Rev. 66 (2014) 040802.
- [2] M. Nouh, O. Aldraihem, A. Baz, Wave propagation in metamaterial plates with periodic local resonances, J. Sound Vib. 341 (2015) 53-73.
- [3] P.A. Deymier, Acoustic Metamaterials and Phononic Crystals, Vol. 173, Springer Science & Business Media, 2013.
- [4] P.F. Pai, G. Huang, Theory and Design of Acoustic Metamaterials, SPIE Press, 2015.
- [5] H. Al Ba'ba'a, M.A. Attarzadeh, M. Nouh, Experimental evaluation of structural intensity in two-dimensional plate-type locally resonant elastic metamaterials, J. Appl. Mech. 85 (4) (2018).
- [6] K.H. Matlack, A. Bauhofer, S. Krödel, A. Palermo, C. Daraio, Composite 3D-printed metastructures for low-frequency and broadband vibration absorption, Proc. Natl. Acad. Sci. 113 (30) (2016) 8386–8390.
- [7] M.A. Attarzadeh, J. Callanan, M. Nouh, Experimental observation of nonreciprocal waves in a resonant metamaterial beam, Phys. Rev. A 13 (2) (2020) 021001.
- [8] Z. Liu, X. Zhang, Y. Mao, Y.Y. Zhu, Z. Yang, C.T. Chan, P. Sheng, Locally resonant sonic materials, Science 289 (2000) 1734-1736.
- [9] L. Liu, M.I. Hussein, Wave motion in periodic flexural beams and characterization of the transition between bragg scattering and local resonance, J. Appl. Mech. 79 (1) (2012).
- [10] H. Al Ba'ba'a, M. Nouh, T. Singh, Formation of local resonance band gaps in finite acoustic metamaterials: A closed-form transfer function model, J. Sound Vib. 410 (2017) 429-446.

[11] E. Baravelli, M. Ruzzene, Internally resonating lattices for bandgap generation and low-frequency vibration control, J. Sound Vib. 332 (25) (2013) 6562–6579.

- [12] P. Wang, F. Casadei, S. Shan, J.C. Weaver, K. Bertoldi, Harnessing buckling to design tunable locally resonant acoustic metamaterials, Phys. Rev. Lett. 113 (1) (2014) 014301.
- [13] C. Liu, C. Reina, Broadband locally resonant metamaterials with graded hierarchical architecture, J. Appl. Phys. 123 (9) (2018) 095108.
- [14] C. Sugino, S. Leadenham, M. Ruzzene, A. Erturk, On the mechanism of bandgap formation in locally resonant finite elastic metamaterials, J. Appl. Phys. 120 (2016) 134501.
- [15] H. Peng, P.F. Pai, Acoustic metamaterial plates for elastic wave absorption and structural vibration suppression, Int. J. Mech. Sci. 89 (2014) 350–361.
- [16] A.O. Krushynska, V.G. Kouznetsova, M.G.D. Geers, Towards optimal design of locally resonant acoustic metamaterials, J. Mech. Phys. Solids 71 (2014) 179–196.
- [17] A.O. Krushynska, M. Miniaci, V.G. Kouznetsova, M.G.D. Geers, Multilayered inclusions in locally resonant metamaterials: Two-dimensional versus three-dimensional modeling, J. Vib. Acoust. 139 (2) (2017).
- [18] P.F. Pai, Metamaterial-based broadband elastic wave absorber, J. Intell. Mater. Syst. Struct. 21 (5) (2010) 517-528.
- [19] H. Sun, X. Du, P.F. Pai, Theory of metamaterial beams for broadband vibration absorption, J. Intell. Mater. Syst. Struct. 21 (11) (2010) 1085–1101.
- [20] D. Krattiger, M.I. Hussein, Bloch mode synthesis: Ultrafast methodology for elastic band-structure calculations, Phys. Rev. E 90 (6) (2014) 063306.
- [21] M.I. Hussein, Phononics: Structural dynamics of materials, iMechanica (2012) (Journal Club Theme of April 2012), https://imechanica.org/node/12210.
- [22] K.-J. Bathe, E.N. Dvorkin, A four-node plate bending element based on Mindlin/Reissner plate theory and a mixed interpolation, Internat. J. Numer. Methods Engrg. 21 (2) (1985) 367–383.
- [23] C.M. Wang, G.T. Lim, J.N. Reddy, K.H. Lee, Relationships between bending solutions of Reissner and Mindlin plate theories, Eng. Struct. 23 (7) (2001) 838–849.
- [24] W. Yu, Mathematical construction of a Reissner-Mindlin plate theory for composite laminates, Int. J. Solids Struct. 42 (26) (2005) 6680-6699.
- [25] S.S. Rao, Vibration of Continuous Systems, John Wiley & Sons, Inc., Hoboken, New Jersey, 2007.
- [26] J.L. Crassidis, J.L. Junkins, Optimal Estimation of Dynamic Systems, CRC Press, Taylor & Francis Group, Boca Raton, Florida, 2012.
- [27] W. Qian, Z. Yu, X. Wang, Y. Lai, B.B. Yellen, Elastic metamaterial beam with remotely tunable stiffness, J. Appl. Phys. 119 (5) (2016) 055102.
- [28] Y. Hu, Z. Guo, A. Ragonese, T. Zhu, S. Khuje, C. Li, J.C. Grossman, C. Zhou, M. Nouh, S. Ren, A 3D printed molecular ferroelectric metamaterial, Proc. Natl. Acad. Sci. (2020).
- [29] M.A. Nouh, O.J. Aldraihem, A. Baz, Periodic metamaterial plates with smart tunable local resonators, J. Intell. Mater. Syst. Struct. 27 (13) (2016) 1829–1845.
- [30] Z. Chen, J. He, G. Wang, Vibration bandgaps of piezoelectric metamaterial plate with local resonators for vibration energy harvesting, Shock Vib. 2019 (2019).